International Journal of Hydrogen Energy 49 (2024) 1160–1175

Contents lists available at ScienceDirect

International Journal of Hydrogen Energy

journal homepage: www.elsevier.com/locate/he

Assessment of MILD combustion in co/counter-swirl configuration using syngas as a fuel

Atanu Dolai *, R.V. Ravikrishna

Combustion and Spray Laboratory, Department of Mechanical Engineering, Indian Institute of Science, Bangalore, 560012, India

ARTICLE INFO

Keywords:
Moderate or intense low oxygen dilution (MILD)
Co/counter-swirl
Non-premixed mode
Planar laser-induced fluorescence (PLIF)
Particle image velocimetry (PIV)

ABSTRACT

Moderate or intense low oxygen dilution (MILD) combustion is investigated in a co/counter-swirl using OH*-chemiluminescence, species measurements, OH planar laser-induced fluorescence (OH-PLIF), two-dimensional particle image velocimetry (2D-PIV), and microphone measurements. Experiments are performed in a two-stage combustor, where the first stage of combustor is catalytic stage and the second stage is the swirl stage (co/counter-swirl configuration). A fuel-rich syngas (20 % H_2, 20 % CO, 12 % CO_2, 2 % CH_4, and 46 % N_2) reacts with air in the catalytic stage. Then, the mixture of unconsumed syngas and products of catalytic combustion is supplied to the swirl stage where the mixture is burnt with oxidizer with varied oxygen concentration. The flame in the swirl stage is established by two concentric swirling streams where the inner stream is the hot gases from the catalytic stage, and the outer stream is the oxidizer. Co/counter-swirl flames are generated by changing the swirl direction of the inner stream. After achieving a stable flame, the macrostructure, flame steadiness, CO and NO_x emissions, reaction zone distribution, and sound pressure level (SPL) are investigated at several oxygen concentrations (O_2 = 13.13 %–21 %) with an aim to assess the MILD combustion mode in co/counter-swirl configuration.

As the oxygen percentage decreases, the flame luminosity decreases for both co/counter-configuration. However, the reduction in luminosity is profound for co-swirl configuration. Clear distinctions between co and counter-swirl configurations are observed regarding flame height and stand-off height. Two-dimensional particle image velocimetry (2D-PIV) is utilized to understand these trends. The steadiness of the flame is investigated using standard deviations (SD) of OH*-chemiluminescence images and global luminosity ($I(t)$). The flame steadiness is found to be improved as the oxygen concentration decreases. The OH-PLIF indicates the distributed nature of combustion. The NO_x emission is found to be extremely low in all studied cases; however, the CO emission shows an increasing trend when O_2 reduces. Finally, the sound pressure level and the dynamics stability are investigated using microphone measurements. The SPL decreases by ~3 dB and ~7 dB for the counter-swirl and co-swirl configuration, respectively. Furthermore, the frequency domain analysis suggests that the fundamental axial mode of the combustor is excited at high oxygen concentration. However, the unsteady combustion and chamber acoustics become decoupled at lower O_2 concentrations. Thus, the present paper, for the first time, confirms that MILD combustion can be achieved in co/counter-swirl configuration, provided the oxygen concentration is low (~13 %). The present study also establishes that the co-swirl configuration is more suitable than the counter-swirl for achieving the MILD combustion mode.

1. Introduction

In recent years, the development of low-emission combustion strategies has been the central theme of combustion research in order to meet strict emission standards. Lean-premixed combustion [1,2], rich-burn quick-quench lean-burn [3–5], catalytic combustion [6,7], moderate or intense low oxygen dilution combustion (MILD) [8–10] are among such few promising combustion strategies. All these strategies have their advantages and disadvantages. Among these, the MILD combustion mode has several desirable characteristics, such as low emissions and improved stability. It is often characterized by uniform temperature distribution, homogenization of reaction zones, and low sound pressure level [11]. Other concepts such as flameless combustion (FC) [11], flameless oxidation (FLOX®) [12], colorless distributed

* *Corresponding author.*
E-mail address: atanu2296@gmail.com (A. Dolai).

https://doi.org/10.1016/j.ijhydene.2023.10.130
Received 10 August 2023; Received in revised form 29 September 2023; Accepted 12 October 2023
Available online 25 October 2023

combustion (CDC) [13,14], and high-temperature air combustion (HiTAC) [15] share many common features with MILD combustion. Thus, in the present study, we use the above concepts interchangeably and adopt the acronym 'MILD' as combustion happens in a low-oxygen environment.

Historically, the MILD combustion regime was first observed by Wünning and Wünning [12] while working with industrial furnaces, although they referred to the regime as flameless oxidation (FLOX®). After that, the combustion regime is explored using simple canonical flames [16–18], reverse flow combustor [8,19,20], and swirl combustor [21,22]. Canonical flames simplify the measurements and simulation owing to their symmetry. Dally et al. performed one of the first studies on canonical Jet-in-Hot-Coflow [16]. They investigated the flame with single-point Raman-Rayleigh-laser-induced fluorescence techniques using CH_4/H_2 as a fuel and highly diluted oxidizer ($O_2 = 3$–9 %). At such low O_2 concentrations, the flame luminosity, peak flame temperature, OH, and CO levels decreased substantially. Using the same configuration, Medwell et al. [23] showed the broadening of OH distribution, although the peak concentration decreases in the oxygen-deficit environment. Partial premixing or the transport of O_2 through the reaction zone is also suggested at such low oxygen concentrations [24]. Compared to atmospheric pressure, Proud et al. [25] showed that an increase in pressure has a similar impact on OH* and CH*-intensity as a reduction in O_2 concentration. The decrease in OH*-chemiluminescence intensity is because of a different OH* formation pathway rather than an increased quenching rate at elevated pressure. It should be also noted that the OH concentration is fuel-specific. For example, the OH concentration is lower for $CH_4/H_2/NH_3$ flames compared to CH_4/H_2 flames at MILD conditions [26].

Besides canonical flames, several researchers investigated MILD combustion using a laboratory-scale combustor. Li et al. [27] performed experiments using a laboratory-scale furnace and observed near-zero CO emissions at MILD conditions. Pramanik et al. [8] achieved the MILD combustion regime using reverse flow combustion and reported that the reaction zone was volumetric and distributed when the oxygen concentration in the oxidizer stream was 7.6 vol%. They also reported negligible NO_x emission (<1 ppm) and very low CO emission (~300 ppm). A similar study performed by Veríssimo et al. [28] showed that the OH* radicals were uniformly distributed over the combustor while operating in MILD conditions, and the normalized NO_x and CO emissions were 10 ppm and 12 ppm, respectively. Although the flame appeared volumetric, slightly luminous, and transparent, it was not entirely flameless or colorless in these studies. Similar observations can be found in the work by Reddy et al. [29] and Arghode et al. [13]. Apart from a reduction in flame luminosity, the combustion stability increases in MILD conditions. Pramanik et al. [8] utilized high-speed OH*-chemiluminescence to assess the stability of the combustion process. They found that the standard deviation (SD) of chemiluminescence intensity was lower in MILD combustion, indicating improved combustion stability. Reddy et al. [29] found that the sound pressure level (SPL) reduced by ~8 dB when the combustion mode was shifted from conventional to MILD. Similarly, Sharma et al. [30] also observed a reduction in decibel levels. Recently, Pramanik et al. [31] performed OH-planar laser-induced fluorescence (PLIF) to inspect the distribution of reaction zones, and they found that the reaction zone was volumetric in the MILD conditions. The NO production and destruction were thoroughly investigated by Li et al. [32] numerically and experimentally. They observed that NO is generated mainly through the N_2O-intermediate route in MILD combustion, and most of the produced NO is consumed through various pathways.

The characteristics of MILD combustion, such as low emissions, high combustion stability, low SPL, and distributed reaction zones are experimentally verified. However, achieving such a combustion mode in practical combustors poses several challenges. To achieve the MILD combustion regime, Cavaliere and de Joannon [33] argued that the reactant inlet temperature (T_{in}) must be higher than the auto-ignition temperature (T_{auto}) and the temperature rise (ΔT) due to combustion should be less than the auto-ignition temperature. Thus, the inlet temperature is one of the crucial parameters for MILD combustion. In our previous study with a reverse flow combustor, we found that the MILD combustion regime was achieved when the preheat temperature was above 724 K, below which the combustion became unstable [34]. Besides inlet temperature, the recirculation of product gases is also essential for many systems. Prior to combustion, the fresh reactants can mix with combustion products to create high-temperature low oxygen conditions. Thus, it is possible to attain the MILD regime despite having a low reactant temperature. However, the product gases should mix with the reactant within a limited ignition delay time [35]. The ignition delay time is lower for fuel with higher hydrogen concentration. Ignition time decreases even further if the reactant is preheated. Thus, MILD combustion can be achieved using hydrogen-containing fuels provided the recirculation of the product gases or the recirculation ratio is high. However, for a swirl combustor, the recirculation ratio is generally low [36]; thus, achieving the MILD regime using such a combustor is even more challenging.

Very few research studies discussed MILD combustion in a swirl combustor. One of the earlier studies on MILD combustion in swirl-stabilized combustors was reported by Khalil et al. [37]. The authors termed the combustion mode as 'colorless distributed combustion' (CDC). Khalil et al. [37] performed experiments using methane as fuel in a combustion chamber with a length of 290 mm, and the swirl number is 0.67. They stabilized the swirl flame in a premixed mode where the oxygen percentage was varied by adding N_2 and CO_2. They reported a substantial reduction in flame luminosity when the oxygen percentage was reduced. The bluish swirl flame became almost invisible at $O_2 = 15$ %. The corresponding OH* chemiluminescence suggested a distributed nature of the combustion. The profound reduction (~90 %) in NO_x emission is reported when O_2 concentration changes from 21 % to 15 %. They reported almost zero CO emissions under MILD conditions. Khalil et al. [21] investigated the MILD combustion regime using particle image velocimetry (PIV) and planar laser-induced fluorescence (PLIF). They found a stark difference in OH radical distribution between conventional and distributed swirling flames. The OH radicals are primarily found in the shear layer between the inner recirculation zone, and the incoming stream for conventional swirl flows. However, the radicals were pushed to the low-velocity region in MILD combustion. Very few literatures discuss the effect of fuel composition on such combustion regime. Khalil et al. [38] experimented with fossil and biomass fuels in a swirl combustor, and they found that the combustion process resembled a well-stirred reactor characterized by a low Damköhler number (Da). Recently, Feser et al. [39] reported distributed swirl combustion using propane as fuel. They found that the transition from conventional to distributed occurred when the N_2 concentration was 15 %. The distributed combustion can be achieved using CO_2 as a diluent. As CO_2 has a higher heat capacity, distributed combustion can be achieved at a higher O_2 concentration [40]. Apart from a reduction in flame luminosity, distributed combustion is beneficial as it reduces combustion noise. Khalil et al. [40] found that the sound pressure level (SPL) was reduced by 17 dB when the combustion mode changed from conventional to distributed. Zhang et al. [41] simulated the distributed combustion using large eddy simulation (LES) with biomass. They found two sets of coherent structures in distributed combustion mode, where the first set corresponded to the vortex shedding resulting from the shear layer instability, and the second set represented the precessing vortex core (PVC).

A review of the literature has helped identify key gaps in the literature. First, all experiments with the swirl combustor were conducted in premixed mode, which means the fuel and oxidizer were mixed before entering the combustion chamber. Secondly, experiments are typically performed in a combustor with a single swirler configuration. Compared to a single swirler, a twin-swirler or co/counter-swirl configuration is superior in terms of mixing, which is a key parameter to achieve the

MILD combustion regime. However, no study discusses MILD combustion in non-premixed mode using a co/counter-swirl configuration. Thus, the present study addresses a very important gap in the literature. Furthermore, the study aims to provide a detailed investigation highlighting the difference and complexity of co and counter-swirl configurations for low outer-to-inner area ratio.

Thus, the present study assesses the feasibility of achieving the MILD combustion regime using a co/counter-swirl configuration by reducing the oxygen concentration of the oxidizer stream. During experiments, a mixture of syngas and air is supplied to the catalytic stage. Syngas is partially consumed, and the mixture of unburnt syngas and catalytic combustion products is supplied to the swirl stage. The species concentrations of the mixture at the catalytic stage's exit are reported in our previous study [42]. This mixture is burnt with an oxidizer with various oxygen concentrations in the swirl stage. In contrast to the previous work [42], a mixture of air and N_2 is used as an oxidizer, and the total flow rate is also kept constant. The paper focuses on the flame shape, luminosity, OH radical distributions, and sound pressure level of the co/counter-swirl flames in the swirl stage at various O_2 concentrations.

The paper contains a detailed description of the two-stage combustor, flowlines, experimental conditions, and a discussion of the measurement techniques followed by a discussion of the results and finally summarizing several key findings of the study.

2. Experimental details

2.1. Experimental setup and flowlines

Fig. 1(a) shows the experimental setup, which is divided into two stages: the catalytic stage (stage 1) and the swirl stage (stage 2). A mixture of biomass-derived syngas (20 % CO, 20 % H_2, 12 % CO_2, 2 % CH_4, 46 % N_2 by volume) and air (21 % O_2 and 79 % N_2) with an equivalence ratio (Φ_{first}) of 4 is supplied to the catalytic stage. Syngas and air are mixed far upstream of the catalytic stage to ensure the gases are entirely mixed. The fuel is consumed partially because of the catalytic combustion in stage 1 (catalytic stage). The remaining unconsumed syngas are combusted with an oxidizer with varying oxygen concentrations in the swirl stage. Understanding the flame characteristics in the swirl stage by changing the O_2 concentration from 13.13 % to 21 % is the primary objective of the present work. Furthermore, the feasibility of achieving MILD combustion at low O_2 concentration is explored.

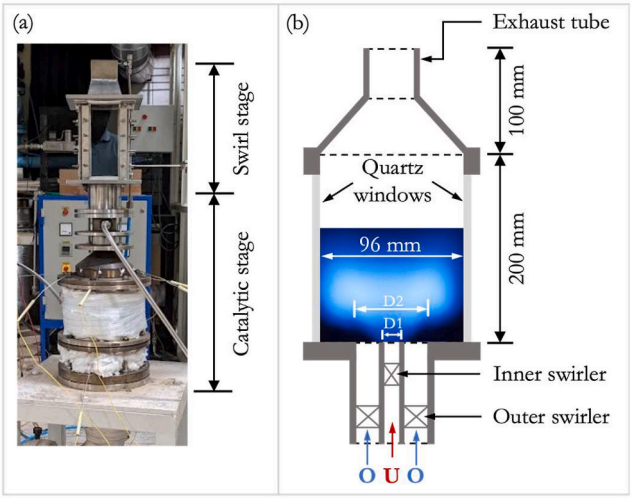

Fig. 1. (a) The two-stage combustor highlighting the catalytic and swirl stage, **(b)** the schematic of the swirl stage with necessary dimensions showing injector configuration, quartz windows, and exhaust tube, where D1 and D2 are 28 mm and 48 mm ('U' represents the mixture of unburnt syngas and catalytic combustion products, and 'O' indicates the oxidiser).

The details of the catalytic stage can be found in our previous study [6,42,43]. A FeCr-alloy monolith coated with Pt catalysts is kept inside the combustion chamber, and the catalysts facilitate combustion inside the monolith channels.

Fig. 1(b) shows the schematic of the swirl stage, which is an optically accessible square chamber. The chamber walls are made of quartz, supported by steel columns at the corner. Quartz plates are chosen because of their low absorptivity. The combustion products leave the swirl stage through the exhaust tube, which is made of stainless steel. As the cross-section of the exhaust tube is smaller than the chamber's cross-section, the gases exit at a higher velocity, preventing any air entrainment from the surrounding. The injector of the swirl stage consists of two concentric tubes: inner and outer tubes. The mixture of catalytic combustion products and unconsumed syngas flows through the inner tube, whereas the oxidizer passes through the outer tube. Swirling motion is imparted on both inner and outer streams using two separate swirlers positioned inside the tubes. Co-swirl flow fields are established when the swirling directions are the same for both streams. In contrast, the swirling direction of the inner stream is opposite to the outer stream for counter-swirl configuration. The geometric swirl number is obtained for the inner and outer streams individually using the following equation [44],

$$SN = \frac{2}{3} tan\,\theta \frac{1-\left(\frac{r_1}{r_2}\right)^3}{1-\left(\frac{r_1}{r_2}\right)^2} \quad (1)$$

where r_1 and r_2 are the inner and outer radius and vane angle is denoted by θ. The dimensions of r_1 and r_2 are 14 mm and 24 mm, respectively. The geometric swirl number for the inner tube (SN_{in}) is 0.67 for the co-swirl, whereas the swirl number is −0.67 for counter-swirl configurations. However, the swirl number for the outer tube (SN_{out}) is kept constant at 0.83 in the present study.

Fig. 2 shows the schematic of the flowlines along with the experimental setup. During experiments, we supplied a preheated and fuel-rich syngas-air mixture ($\Phi_{first} = 4$) to the catalytic stage. An electrical heater (power rating = 5 kW) was used to preheat the syngas-air mixture to the desired temperature. Catalytic combustion occurred on the surface of the platinum catalysts embedded on the monolith walls when the syngas-air mixture was supplied. The mixture of unburnt syngas and product gases from the catalytic stage flowed continuously through the inner tube. When the temperature at the outlet of the monolith reached a steady value, an oxidizer with $O_2 = 21$ % and a flow rate of 400 SLPM was supplied through the outer tube. The mixture of unburnt gases and oxidizer was then ignited using a flame torch. Once the flame was established, the oxygen percentage of the oxidizer stream was changed

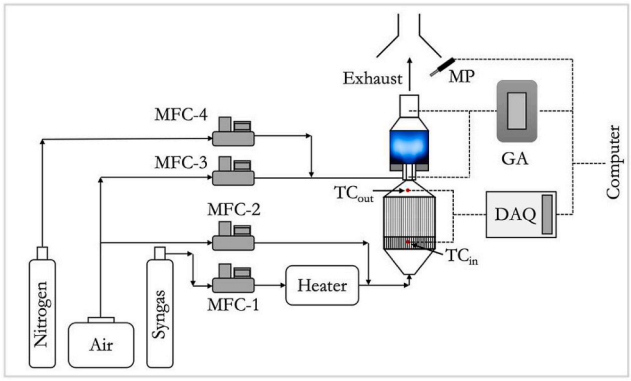

Fig. 2. The graphical representation of the flowlines (acronyms: MFC→ mass flow controller, GA → gas analyzer, DAQ→ Data acquisition system, TC→ Thermocouple, and MP→ microphone).

by varying the proportion of air and N_2 while keeping the total flow rate constant at 400 SLPM.

For the catalytic stage, the air and syngas flow rates were precisely controlled by two separate mass flow controllers (Make: ALICAT, accuracy: 0.8 % of the reading + 0.2 % of full scale). Mass flow controller (MFC)-1, used for syngas, ranges from 0 to 800 SLPM, and MFC-2 ranges from 0 to 100 SLPM, which is used for air. In the swirl stage, the oxygen percentage in the oxidizer stream was controlled by air and N_2 flow rates. Air and N_2 flow rates were precisely controlled by two separate MFCs, denoted as MFC-3 and MFC-4, respectively, in Fig. 2. Both MFCs range from 0 to 800 SLPM and have accuracy similar to MFC-1.

2.2. Operating conditions

The operating conditions of the stage-1 is crucial as the products of catalytic combustion and unconsumed syngas are supplied to the stage-2. The equivalence ratio for the catalytic stage is chosen such that the maximum temperature inside the monolith is below an allowable temperature (T_{max}). If the monolith inside temperature exceeds the T_{max}, the catalysts may disintegrate from the monolith wall, degrading the monolith performance. The allowable temperature is 1173 K, which is prescribed by the manufacturer. Additionally, catalytic combustion of syngas under fuel-lean conditions is not recommended because of the hydrogen present in the fuel. Hydrogen easily diffuses on the surface of the catalyst and can create hotspots [45]. These hotspots reduce the catalyst life significantly. Thus, we supplied a fuel-rich mixture to the catalytic stage. The equivalence ratio is selected such that the corresponding adiabatic temperature is less than T_{max}. We utilized the equilibrium module in CHEMKIN PRO$^{(R)}$ and GRI 3.0 [46] to calculate the adiabatic flame temperature. It is found that the equivalence ratio should be greater or equal to 4 for safe operation when the inlet temperature is 573 K.

The selection of a catalyst is not straightforward. The reactivity of the catalysts depends on several parameters such as catalyst type, fuel composition, equivalence ratio (fuel-lean vs. fuel-rich), the conductivity of the monolith wall temperature, etc. Among studied catalysts, noble catalysts such as platinum (Pt), palladium (Pd), and rhodium (Rh) are found to be more reactive compared to metal oxides. Pd-based catalyst is more suited for practical combustion owing to its higher reactivity and lower light-off temperature. However, Pd-catalysts often exhibit unpredictable behavior for methane oxidation, such as deactivation and hysteresis in reaction rate at high temperatures due to Pd–PdO catalyst morphology [47,48]. It is also possible to encounter such unpredictable behaviors when CO/H_2 mixtures are used as fuel. Furthermore, for H_2/O_2 mixtures, hydrogen inhibits its ignition at fuel-rich conditions as the active sites on the catalyst surface are covered by H(s), preventing the adsorption of O_2 [49]. Compared to Pd-based catalysts, Pt-based catalysts show lower reactivity. These catalysts also exhibit self-inhibition at higher equivalence ratios for the same reason. However, Pt-based catalysts do not display any deactivation or hysteresis. In contrast to the previous two noble catalysts, the Rh-based catalysts do not self-inhibit hydrogen oxidation and are better suited for hydrogen-containing fuels. However, Mantzaras [49] pointed out that the thermal effects can become significant at higher equivalence ratios for practical combustors, overriding the chemical self-inhibition. Apart from monometallic catalysts, bi-metallic catalysts also have several advantages. For Pd–Pt bi-metallic catalysts, lower ignition and higher reactivity can be achieved because of Pd, whereas Pt provides stability by reducing the possibility of having deactivation or hysteresis of reaction rate. Persson et al. [50] compared the methane conversion under lean fuel-air conditions between palladium-platinum (Pd–Pt) bi-metallic catalysts and palladium (Pd) monometallic catalysts. They found that Pd–Pt showed moderate reactivity at the start compared to Pd-catalysts, but it increased over time. However, the complex surface chemistry of these bi-metallic catalysts has yet to be fully understood. In the present study, we choose platinum catalysts as they have been studied extensively by several studies [51,52].

The operating conditions of the catalytic stage are listed in Table 1, and the flow rates, equivalence ratio (Φ_{first}), and inlet temperature remained unchanged in the study. For the swirl stage, the O_2 concentration in the oxidizer stream is systematically varied from 21 % to 13.13 % with the objective of achieving the MILD combustion regime. The required oxygen percentage to achieve such combustion mode depends on various parameters such as inlet temperature, fuel type, and recirculation ratio. For example, Verissimo et al. [28] used air (21 % O_2, 79 % N_2 by volume) as an oxidizer. They achieved MILD combustion by controlling the mixing between air and fuel jets. Pramanik et al. [8] achieved the MILD combustion regime using syngas (20 % CO, 20 % H_2, and 60 % N_2) when the oxygen concentration in the oxidizer stream was 7.6 % by volume. In jet-in-hot-co-flow (JHC) burners, several researchers studied this combustion regime at extremely low oxygen concentrations (3 %–9 % by volume) [16,23]. Khalil et al. [38,40] investigated the MILD combustion regime using a single-swirl combustor, and they achieved this combustion regime when the O_2 = 15 %. As no study is performed in a twin-swirl configuration, we reduced the oxygen concentration gradually and monitored the CO and NO_x emissions at the exit of the swirl stage. When O_2 concentration is changed from 13.13 % to 11.8 %, although the flame luminosity decreases, a sharp increase in CO emission is observed. The measured CO emission was above 10,000 ppm, considerably higher than the emission norm. Thus, we investigated the combustion mode above 13.13 % by volume in the present study.

The variation in the O_2 concentration is achieved by varying the proportion of air and N_2 while keeping the total flow rate constant. The total flow rate of air (Q_{air}) and N_2 (Q_{N2}) is kept constant at 400 SLPM. The complete experimental conditions are listed in Table 1.

2.3. Measurement techniques

2.3.1. Temperature measurement

Temperatures were measured at several locations using thermocouples. One thermocouple placed upstream of the monolith (radius = 0 mm) measured the inlet temperature. Monolith outlet temperatures were measured using four thermocouples kept at various radial locations. The monolith outlet temperature is crucial as it indicates the temperature of the gases supplied to the swirl stage. We chose *K*-type thermocouples for both inlet and outlet because the expected temperature ranges from 300 K to 1200 K.

2.3.2. Species measurement

Species concentrations were measured at two locations, namely the exit of the catalytic and swirl stages. At the exit of the catalytic stage, samples were collected through a ¼-inch stainless-steel tube. Collected gases were passed through the condenser, where water was extracted. Then the sample was supplied to a gas analyzer (Make: SICK, model: S715), which is capable of measuring CO_2, CO, CH_4, H_2, and O_2.

At the exit of the combustor, a TESTO-350 gas analyzer monitored the CO and NO_x concentrations during experiments. The analyzer's probe was placed at the combustor centerline and 50 mm downstream of the combustor exit plane. The gas analyzer can measure CO, NO_x, and O_2. The range and accuracy of the analyzers can be found in our previous study [42].

2.3.3. Sound measurement

A microphone (Make: PCB 130E20) was used to record the sound emitted from the combustor. The microphone was placed horizontally at the combustor exit plane and 250 mm away from the combustor centerline. Before conducting any experiment, the microphone was calibrated using an acoustic calibrator (Make: PCB, Model: CAL200) with a sound pressure level (SPL) of 94 dB and 114 dB (±0.2 dB) at 1 kHz (±1 %). At each operating condition, the sound was recorded at a frequency of 50 kHz using a data acquisition system (NI-DAQ).

Table 1
List of the experimental conditions (acronyms: LC →low-speed chemiluminescence, HC→ high-speed chemiluminescence, PLIF→ planar laser-induced fluorescence, PIV → particle image velocimetry).

Syngas flowrate (SLPM)	Air flowrate in catalytic stage (SLPM)	Air flowrate in swirl stage (SLPM)	N_2 flowrate in swirl stage (SLPM)	O_2 percentage in the oxidizer stream (%)	Equivalence ratio in the swirl stage (Φ_{swirl})	Configuration	Diagnostic
233	67	400	0	21	0.49	Co-swirl	OH*-HC (5 kHz) + OH*-LC (10 Hz) + OH-PLIF + PIV
					0.49	Counter-swirl	
		375	25	19.69	0.52	Co-swirl	OH*-LC (10 Hz)
					0.52	Counter-swirl	
		350	50	18.37	0.55	Co-swirl	OH*-HC (5 kHz) + OH*-LC (10 Hz) + OH-PLIF
					0.55	Counter-swirl	
		325	75	17.1	0.60	Co-swirl	OH*-LC (10 Hz)
					0.60	Counter-swirl	
		300	100	15.75	0.65	Co-swirl	OH*-HS (5 kHz) + OH*-LC (10 Hz) + OH-PLIF
					0.65	Counter-swirl	
		250	150	13.125	0.78	Co-swirl	OH*-HC (5 kHz) + OH*-LC (10 Hz) + OH-PLIF + PIV
					0.78	Counter-swirl	

2.4. Low-speed OH*-chemiluminescence setup

Apart from temperature, species, and sound measurement, we investigated the change in flame macrostructure when the O_2 percentage decreases using a low-speed (10 Hz) OH*-chemiluminescence imaging. Images were captured using a CCD camera (Make: Lavision, Model: Imager SX) equipped with intensified relay optics (Make: Lavision) and a UV lens. A bandpass filter centered around 308 nm (FWHM = 10 nm) was attached to the UV lens (Make: Nikkor, focal length = 105 mm, aperture (f) = 2.8) to remove the unwanted wavelength. The exposure time for each image was set to ~1 ms, and the flame macrostructure was obtained by averaging 400 images.

2.5. High-speed OH*-chemiluminescence setup

The high-speed OH* chemiluminescence experimental setup consisted of high-speed intensified relay optics (Make: Lavision), a CMOS camera (Make: Photron, Model: Fastcam), and a UV lens fitted with a bandpass filter (308 nm ± 10 nm). A programmable timing unit (Make: Lavision, PTU V9) provided the triggering signal to all components. During experiments, the exposure time was kept to 60 μs, and images were recorded at a frequency of 5 kHz for 1 s.

2.6. Laser diagnostics

2.6.1. Planar laser-induced fluorescence (PLIF) of OH radicals

Planar laser-induced fluorescence (PLIF) was utilized to investigate the OH radical distribution at various oxygen concentrations. The schematic for the setup for OH-PLIF experiments is shown in Fig. 3(a). The experimental setup consisted of two main components: Nd:YAG laser and dye laser. A Nd:YAG laser supplied the laser beam with a wavelength of 532 nm at 10 Hz. Two dichroic mirrors directed the laser beam into the dye laser (Make: Sirah Lasertechnik). We obtained a laser beam with a wavelength of 283.55 nm at the outlet of the dye laser. Thus, the radicals were excited by the Q1(8) line belonging to the OH spectra's $A^2\sum+ \rightarrow X^2\prod$ (1,0) band. The output of the dye laser was converted into a parallel laser sheet using a collimator and sheet optics. The height and thickness of the sheet were ~47 mm and ~0.5 mm, respectively. A single laser sheet was not sufficient to obtain useful information because the flame height reached up to 80 mm in some conditions. Thus, the laser sheet was moved at three axial locations during the experiments to span the entire flame. We made a mirror arrangement in order to change the laser sheet location vertically. The sheet optics, energy monitor, and collimator were kept on a screw jack and two UV mirrors were placed at the exit of the dye laser, which directed the output beam to sheet optics. By rotating the screw jack, the sheet was obtained at different axial locations. Fig. 3(b) shows the laser sheets at three axial locations, which are denoted as L1, L2, and L3 in figure. A sufficient overlap was provided among the sheets, which helped in combining the three average images. The laser energy at the output of the dye laser was always checked prior to the experiments, and the energy was maintained at ~25 mJ/pulse.

The fluorescence signal at this energy was found to be in the linear region. At this transition, the Boltzmann fraction is insensitive to the variation in the gas temperature (<10 %). The fluorescence was recorded using a CCD camera. As the signal intensity is extremely low, the

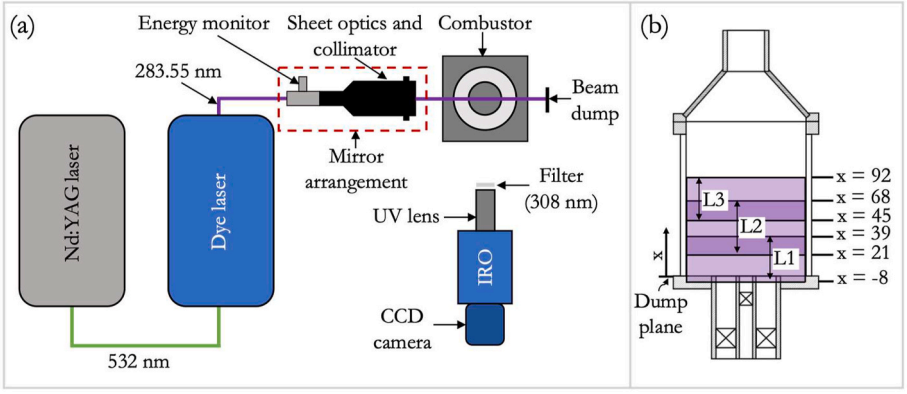

Fig. 3. (a) The schematic of different components used for OH-PLIF experiments, **(b)** The axial locations of the three laser sheets, denoted as L1, L2, and L3 with respect to the dump plane.

incoming fluorescence signal was increased using intensified relay optics (IRO, Make: Lavision), which is connected to the CCD camera. Additionally, a UV lens and a 308 nm (FWHM = 10 nm) bandpass filter were connected with IRO to capture only the OH fluorescence signal. The intensifier opening time was kept constant at 50 ns. To get the complete radical distribution, 200 images were recorded at 10 Hz at three different axial locations for all experimental conditions. As part of the post-processing, all the raw images were corrected for pulse-to-pulse energy variation and nonuniformity of the sheet energy profile.

2.6.2. Particle image velocimetry (PIV)

Two-dimensional particle image velocimetry (2D-PIV) was used to obtain two components of the velocities (U) at the midplane of the combustor. Instantaneous velocity field was acquired at a frequency of 5 Hz. Fig. 4(a) shows the schematic of the experimental setup. A Nd:YAG laser provided a high-intensity dual-pulsed laser beam with a wavelength of 532 nm. The circular laser beam was transformed into a sheet using sheet optics. In the present study, Alumina particles with a mean diameter of 1 μm were used as seeding particles. The Stokes' number corresponding to such particles was found to be extremely low, which ensures that the particles follow the actual velocity field. The interval between two pulses was set between 10μs and 20μs. The scattering from the seeding particles was recorded using a CCD camera (Make: Lavision, Model: Imager Pro X). The CCD camera was equipped with a Nikkor lens (focal length = 105 mm, f5.6) and a bandpass filter (532 nm ± 10 nm). The resolution of the camera was 2048 pixels × 2048 pixels. The velocity was computed from two frames using Davis software using standard cross-correlation methods and an interrogation window of 32 pixels × 32 pixels (two passes) with an overlap of 75 %. Based on the uncertainty of cross-correlation algorithm, the random uncertainty of the measurement was found to be ±0.57 m/s. At each experimental condition, 200 images were captured to obtain several statistical quantities of the velocity field.

3. Results and discussions

3.1. Temperature and species concentrations at the exit of the catalytic stage

As stated before, the temperature and species concentrations at the catalytic stage's exit are important parameters that influence the flame structure and emissions in the swirl stage. Thus, we begin by discussing the temperature profiles at the inlet and outlet of the catalytic stage briefly. Fig. 5(a) shows the evolution of the temperature profiles with time, where the blue line denotes the monolith inlet temperature (r = 0 mm), and the red lines denote the outlet temperatures at four radial

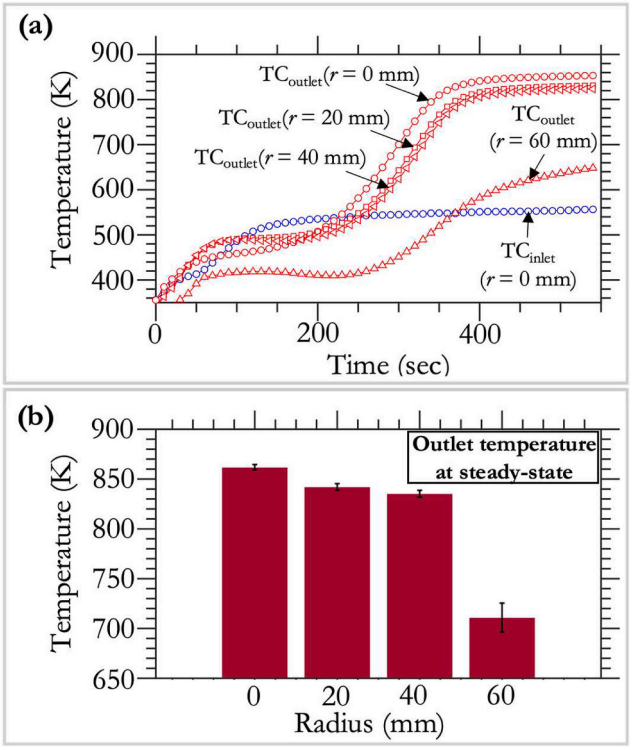

Fig. 5. **(a)** The temperature evolution at the inlet and outlet of the monolith, **(b)** the temperature variation in the radial direction at steady state.

locations. The monolith outlet temperature starts to increase as soon as the premixed syngas-air mixture is supplied. As evident from the figure, the outlet temperatures (r < 60 mm) reach a steady state within 400 s. However, the temperature measured at r = 60 mm, takes longer to reach a steady state because of the heat loss to the combustor wall. Fig. 5(b) shows the radial temperature distribution at the monolith outlet at a steady state. Temperature is almost uniform within a 40 mm radius from the center, and the temperature variation is only 20 K. However, the temperature decreases significantly after r = 40 mm. The steady-state temperature at r = 60 mm is ~150 K lower than at r = 0 mm. To check the repeatability, the same experiment is repeated several times and we found that the average monolith temperature (r = 0 mm) is ~860 K, and the deviation of the temperature between experiments is found to be small. Fig. 5(b) shows a maximum standard deviation of ~15 K. Thus, it is confirmed that the average monolith outlet

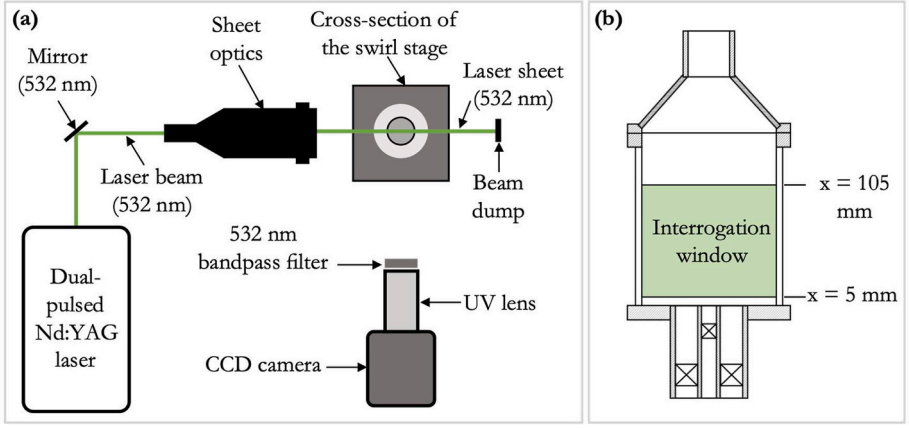

Fig. 4. **(a)** The schematic of the different components used in PIV experiments, **(b)** The schematic of the swirl stage showing the field of view of PIV experiments (field of view = 80 mm × 100 mm).

temperatures remain unchanged in all the experiments.

Along with temperature, we also verified that the species composition remains unchanged in all experiments. As the gases from the catalytic stage are supplied to the swirl stage, the species concentrations indicate the composition of the gas flowing through the inner tube. We performed species measurements four times, and the average concentrations of the main species are listed in Table 2. The standard deviation is extremely small compared to the accuracy of the measuring device. Thus, we considered the accuracy of the measuring device as the error in the experiment. The accuracy of the measuring device for different gas species is presented in the previous section. From species concentration, we infer that a portion of syngas is consumed in the catalytic stage. Apart from CO and H_2, a significant amount of CO_2 and N_2 is also present in unburnt gas. Additionally, we found a trace amount of methane (CH_4) and oxygen (O_2) at the catalytic stage's exit. Apart from the mean concentrations, the percentage conversion of CO, H_2, CH_4, and O_2 is also listed in Table 2. A more detailed description of the concentration measurement can be found in our previous study [42].

In summary, the catalytic stage partially consumes the syngas-air mixture because of hetero-/homogeneous combustion occurring inside the monolith channels. A detailed investigation of the combustion process inside a single channel is impossible in the present study, as the monolith is placed inside a catalytic stage. However, a study by Bolanos-Chaverii et al. [53] indicates that heterogeneous and homogeneous combustion can occur in the channel for fuel-rich conditions. The consumption of limiting species O_2 on the catalysts' surface is slower due to its lower diffusivity, allowing H_2 and CO to be consumed through several gaseous pathways. As a result of the hetero-/homogeneous combustion, the monolith outlet temperatures increase. At steady-state, the temperature at the outlet is high, ~860 K, at $r = 0$ mm. Thus, the catalytic stage helps in producing high-temperature unburnt gases, which is beneficial for achieving MILD combustion. The unburnt gas contains a significant amount of CO, H_2, CO_2, CH_4, H_2O, and N_2, which is supplied to the swirl stage. A small amount of O_2 is also present in species composition. We infer that the incomplete combustion inside the channels situated in the vicinity of the combustor wall is the source of this oxygen. The steady-state temperature profile indicates that the temperature is maximum in the monolith center and drops sharply when $r > 40$ mm. This drop in temperature is due to the heat loss from the monolith to the combustor wall. Thus, the consumption of oxygen is significantly affected in the channels near the combustor wall; as a result, a small amount of O_2 is present in the species concentration.

The high-temperature unburnt gas from the catalytic stage is combusted with an oxidizer, and the impact of the oxidizer's O_2 concentration on the flame macrostructure, emission, and stability are discussed in the following sections. Furthermore, the feasibility of achieving MILD combustion in the swirl stage is assessed based on OH*-chemiluminescence intensity, the steadiness of the reaction zone, the distribution heat release zone, and the sound pressure level (SPL).

3.2. Mean-OH* chemiluminescence of co/counter-swirl flames in swirl stage

The flame in the swirl stage is ignited with an oxidizer with 21 % O_2 when the monolith outlet temperature reaches a steady state. After establishing a stable flame, the O_2 concentration of the oxidizer stream is systematically reduced to 13.13 %. We utilize OH*-chemiluminescence, which is extensively used in literature to investigate the flame structure and reaction zone [8,37].

Table 2
The steady-state species concentrations at the exit of the catalytic stage.

Species	CO (%)	CO_2 (%)	O_2 (%)	CH_4 (%)	H_2 (%)
Mole fraction	13.74	12.6	0.29	0.98	11.82
Conversion (%)	11.7	–	93.8	37	24

The averaged OH*-chemiluminescence for co/counter-swirl flames at different O_2 concentrations is shown in Fig. 6. At $O_2 = 21$ %, the co-swirl configuration produces a 'Trumpet'-shaped flame. The highest OH*-chemiluminescence intensity is observed at ~35 mm from the dump plane. At axial location (x) = 35 mm, the intensity increases until radius (r) = 30 mm from the centerline, then decreases near the chamber wall. The same intensity profile can be observed at all axial locations except close to the dump plane. The central region has relatively low OH* intensity, possibly due to product gas recirculation which happens because of the adverse pressure gradient created by two swirling steams. The angular momentum of the inner and outer streams changes along the axial direction because of the difference in velocity magnitude and sudden expansion. The outer oxidizer stream tries to reduce the momentum of the inner stream. This decay in momentum generates an adverse pressure gradient which recirculates the burnt gases. Thus, the central region is expected to be filled with burnt gases, and low intensity is because of the low concentration of OH radicals. The recirculation of gases helps in flame stabilization as the hot burnt gases mix with fresh incoming streams. At the same oxygen concentration, the counter-swirl forms a distinct and more compact flame than the co-swirl. The chemiluminescence image shows a highly luminous central region and the highest intensity is located at ~30 mm from the dump plane. The central region is relatively filled with OH radicals compared to the co-swirl configuration. Merkle et al. [54] reported that the counter-swirl creates a compact recirculation zone, whereas the co-swirl creates a long recirculation zone. Thus, the difference in flame shape is attributed to the flow field generated by co/counter-swirl configurations, which is verified in the later sections.

When the O_2 percentage decreases, the chemiluminescence intensity decreases, and the region with the highest luminosity gradually moves away from the dump plane for both configurations. For example, at O_2 = 17.10 %, the location of peak intensity shifts to axial location(x) ~40 mm for co-swirl configuration. In comparison, the peak location moves from ~30 mm to ~40 mm for counter-swirl under the same reduction in oxygen concentration. The OH intensity is lowest when oxygen concentration is 13.13 %, which is expected as the formation of OH radicals depends on the oxygen concentration. For H_2 oxidation, the primary chain-initiation reaction is $H_2 + O_2 \rightarrow HO_2 + H$ at low temperatures [55]. The H-radicals further react with oxygen (O_2) and produce OH-radicals via $H + O_2 \rightarrow OH + O$. Similarly, for CO oxidation, $CO + O_2 \rightarrow CO_2 + O$ reaction provides O-radicals which later react with H_2O or H_2 and produces OH radicals. If OH radicals are present in the reaction zone, CO is mainly converted to CO_2 via $CO + OH \rightarrow CO_2 + H$. Thus, the chain-initiation and chain-branching reactions significantly depend on the oxygen concentration, and the reduction in O_2 concentration directly implies the reduction in OH radicals. Thus, the OH* intensity reduces with O_2 concentration. Moreover, the background emission from CO_2* can play an important role in reducing the luminosity, as suggested by Zhou et al. [56]. It should be worth mentioning that the flame neither becomes invisible nor colorless even though the flame OH* chemiluminescence intensity reduces. In a similar study with a premixed swirl combustor, Feser et al. [39] also reported a reduction in OH*-chemiluminescence intensity when O_2 concentration reduces. However, they have performed experiments with premixed fuel-air mixtures, and the swirl configuration is entirely different from that of the present study.

3.3. Flame height and stand-off distance

Apart from a decrease in OH* intensity, a change in flame height and stand-off distance is observed when O_2 concentration reduces. The flame height is measured by identifying the flame front. We utilized the Otsu thresholding method to obtain the flame front from the average chemiluminescence images [57]. The furthest location of the flame front from the dump plane ($x = 0$ mm) is considered as flame height.

The variation of flame height with O_2 concentration for co/counter-

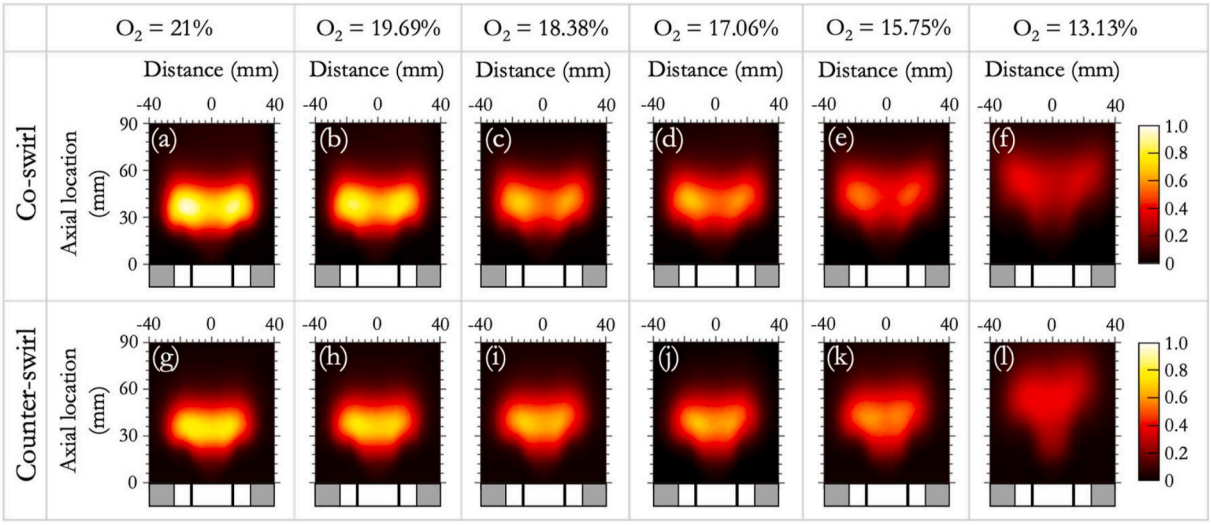

Fig. 6. The averaged OH* chemiluminescence images of co/counter-swirl flames at different O_2 concentrations (images are normalized by the maximum intensity observed at O_2 = 21 %).

swirl configurations is shown in Fig. 7(a). As discussed in the previous section, the counter-swirl flame is smaller than the co-swirl flame at O_2 = 21 %. One of the possible explanations is that the counter-swirl configuration produces a small recirculation zone (RZ) close to the dump plane. Furthermore, the counter-swirl configuration promotes higher mixing, allowing unburnt gases to react with the oxidizer within a shorter distance. As the O_2 percentage decreases, the flame height gradually increases for both configurations till O_2 is ~15.75 %. Additionally, the flame is progressively distributed over a larger volume of the combustor (see Fig. 6). An interesting trend is observed when the O_2 < 15 %. For co-swirl, the flame height increases from ~63 mm to ~74 mm when the O_2 concentration changes from 15.75 % to 13.13 %. Interestingly, a substantial increment is found for the counter-swirl configuration. The flame height becomes ~80 mm at O_2 = 13.13 %, which is larger than that observed in co-swirl at the same condition. In Fig. 7(a), the curve corresponding to K/O_2 is also shown with a dashed line, where K is the proportionality constant. For both configurations, the flame height closely follows the curve, which is expected as the reaction rate and chemical time scale depend on oxygen concentration. The reaction rate decreases when oxygen concentration decreases due to the scarcity of radicals. Thus, the gases require a larger length for complete conversion, indicating that the flame height inversely varies with oxygen concentration. However, the flame height and trend are different for co/counter-swirl configuration at the same O_2 concentration suggesting that the flame height also depends on the flow field apart from chemical kinetics. Thus, in the later section, flow field corresponding to co/counter-swirl flames is studied in detail.

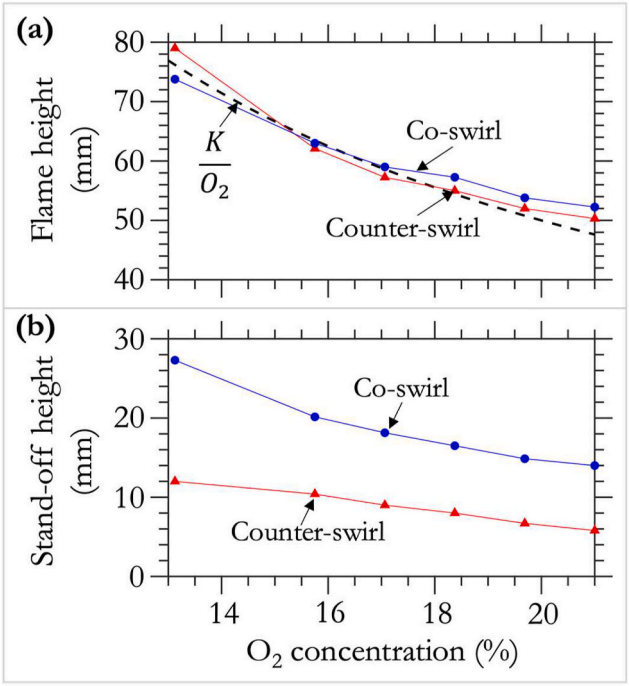

Fig. 7. (a) The variation of flame height with the oxygen percentage in the oxidizer stream where K is a proportionality constant and K = 1, **(b)** the stand-off distance of the flame from the dump plane at different O_2 percentage.

Interesting phenomena are observed in the vicinity of the dump plane. By carefully examining the chemiluminescence images, the flame base is found to be either attached to the dump plane or completely in a lifted state. This motivated us to examine the variation of average stand-off distance at several O_2 concentrations. Flame stand-off distance indicates the distance of the nearest flame front from the dump plane. A different method reported by Sadanandan et al. [58] is adopted to calculate the distance. First, the averaged and normalized chemiluminescence images are binarized using an arbitrary threshold value (0.1 for the present study). After binarization, the distance of the nearest pixel with an intensity of 1 from the dump plane is considered as stand-off distance. Even though the threshold is chosen arbitrarily, the trend obtained after binarization is insensitive to the threshold value [58].

The stand-off distances for co/counter-swirl configurations are shown in Fig. 7(b). At O_2 = 21 %, the co-swirl flame stabilizes mostly away from the dump plane. However, in a few instances, the flame edge moves upstream, and the flame temporarily stays attached to the burner rim. The average stand-off distance is found to be ~14 mm. In comparison, the flame randomly oscillates between attached and lift-off states for counter-swirl configuration, leading to a smaller stand-off distance (~6 mm). As the O_2 concentration changes to 15.75 %, the stand-off distance gradually increases for both configurations. However, a drastic increase in stand-off distance is observed for the co-swirl configuration when O_2 changes from 15.37 % to 13.13 %. The distance becomes approximately 30 mm. In contrast, the stand-off distance slightly increases for counter-swirl under a similar reduction in oxygen concentration. Fig. 7(b) also suggests that the stand-off distance is always smaller for the counter-swirl configuration compared to the co-

swirl configuration. The maximum distance for counter-swirl is ~12 mm, which is smaller than that observed for co-swirl at $O_2 = 21$ %. Thus, it is evident that flame elongates and stand-off distance increases when O_2 concentration decreases, and OH radicals occupy a considerable volume of the combustor. This is different from the conventional swirl flames where the luminous region is concentrated in the shear layer. A low OH*-chemiluminescence intensity and increase in flame height at low O_2 concentration indicate that MILD combustion is possible with co/counter-swirl configuration. Besides intensity and height, the stability of combustion, distribution reaction zone, and emissions are also important parameters for attaining MILD combustion. Thus, we discuss the stability of the combustion using high-speed OH* chemiluminescence in the next section. Then, in the following few sections, the detailed investigation of flame structure using PLIF and PIV and CO and NO_x emissions at various O_2 concentrations are presented.

3.4. Evaluation of unsteadiness using standard deviation and average global luminosity

We adopted two approaches to evaluate the unsteadiness of the co/counter-swirl flames. The spatial unsteadiness can be captured by considering the standard deviation (SD) of chemiluminescence images. Apart from SD, global luminosity ($I(t)$) is evaluated from each chemiluminescence image by averaging the chemiluminescence signal over the spatial domain. The spatial domain (90 mm × 86 mm) is kept the same for all oxygen concentrations. The standard deviation of global luminosity represent the temporal steadiness of the combustion.

Fig. 8 shows the standard deviation (SD) of OH* chemiluminescence images for co/counter-swirl configuration at various O_2 concentrations. In order to understand the change in SD, the images are normalized by the maximum SD found at $O_2 = 21$ %. Figure indicates that the highest SD is found at $O_2 = 21$ % for both configurations. For co-swirl configuration, the highest SD is located at x ~30-mm and ~20-mm away from the combustor centreline, indicating a significant unsteadiness in the location and intensity of the heat release zone. In contrast, the central region also shows a high SD for counter-swirl. The SD decreases when oxygen concentration reduces, and the minimum SD is found when $O_2 =$ 13.13 %, which suggests that the stability and steadiness of the location of the heat release rate increases.

Fig. 9 shows the distribution of $I(t)$ at several oxygen concentrations. For brevity, we consider only four conditions. The distribution is obtained from 5000 instantaneous OH* chemiluminescence images. The mean of the distribution is denoted as μ in the figure. Fig. 9 corroborates the observation found from the flame macrostructure. Similar to the chemiluminescence intensity, the value of μ decreases with a reduction in O_2 concentration. However, it is now possible to quantify the change in OH* intensity using a single parameter. The mean intensity (μ) is highest (49.8 a.u.) for co-swirl configuration at $O_2 = 21$ %. For counter-swirl, the mean intensity is slightly lower, which is 40.6. At $O_2 = 18.37$ %, the value of μ reduces to 45.8 for the co-swirl configuration. Surprisingly, the μ remains unaltered for counter-swirl configuration. As the O_2 percentage decreases further, the mean intensity (μ) decreases for both configurations. It is evident from the mean intensity (μ) that the two configurations behave differently with O_2 concentration. When O_2

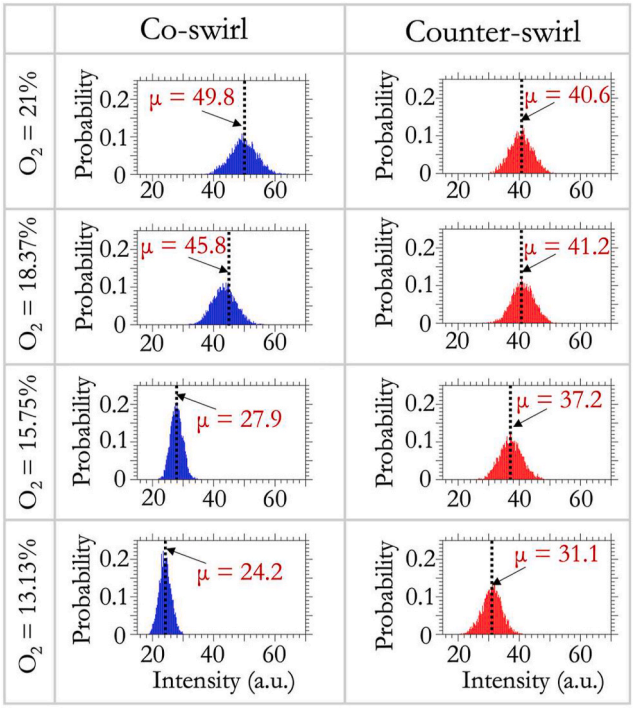

Fig. 9. Distribution of $I(t)$ calculated from instantaneous OH*-chemiluminescence images (frequency = 5 kHz), where μ is the mean intensity (a.u. represents the value of global luminosity in counts).

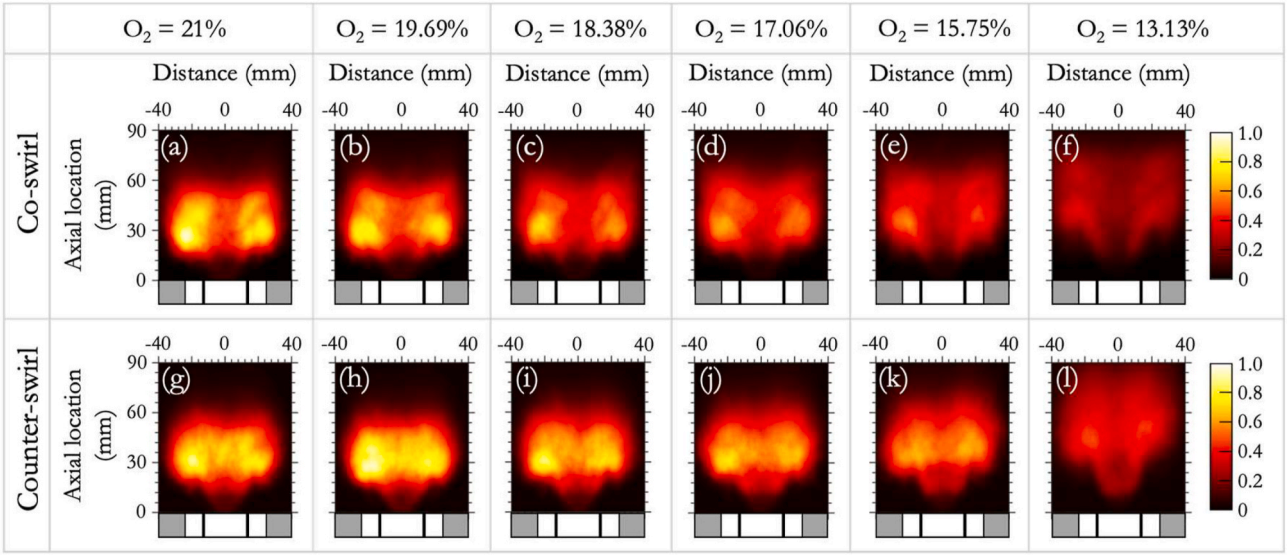

Fig. 8. Standard deviation of OH* chemiluminescence images where the first and second row represent the co-swirl and counter-swirl configuration, respectively (intensity is normalized by the maximum counts found at $O_2 = 21$ %).

decreases from 21 % to 13.13 %, the value of μ for co-swirl reduces from 49.8 to 24.2, which means μ reduces by nearly ~52 %. In comparison, the μ reduces from 40.6 to 31.1 for the counter-swirl configuration under the same reduction in O_2 concentration, which means the reduction is only by ~23 %. Thus, the reduction in chemiluminescence intensity is profound for co-swirl configuration.

Fig. 9 also shows the spread or standard deviation (SD) of global intensity distribution at several O_2 concentrations. At $O_2 = 21$ %, both configurations have the largest standard deviation (SD) of the *I(t)* distribution. The average global intensity distribution resembles a Gaussian distribution closely. A large standard deviation (SD) indicates that the global intensity varies significantly with time, and the combustion process is highly unsteady. The SD shows a decreasing trend with O_2 concentration for co-swirl configuration. SD is minimum at $O_2 = 13.13$ %, indicating the stable nature of the combustion process. In comparison, the SD for counter-swirl configuration follows approximately a Gaussian distribution at all O_2 concentrations, and a slight reduction in SD is found only at $O_2 = 13.13$ %.

In summary, several notable phenomena are observed for co/counter-swirl flames when the O_2 percentage is varied in the oxidizer stream. The flame luminosity decreases, and the flame height increases with a reduction in O_2. The standard deviation (SD) of chemiluminescence images and global luminosity indicate an increase in the steadiness of the reaction zone. Thus, it is possible to achieve MILD combustion in the co/counter-swirl configuration by reducing the O_2 concentration, as suggested by the flame luminosity and SD. However, the heat release rate (HRR) distribution, sound pressure level (SPL), and emissions are other important parameters that need further investigation. The chemiluminescence only provides a line-of-sight integrated intensity of OH radicals, whereas planar laser-induced fluorescence (PLIF) provides a complete picture of radical distribution or heat release zone. Thus, the following sections discuss the influence of O_2 concentration on HRR. At the same time, two-dimensional (2D) particle image velocimetry (2D-PIV) is utilized to explain the difference between co and counter-swirl flames. Finally, the sound pressure level and emissions are discussed.

3.5. Influence of O_2 concentration on heat release rate (HRR)

3.5.1. OH radicals as heat release marker

We conducted counterflow simulations using CHEMKIN PRO© and GRI 3.0 [46] as a reaction mechanism at two global strain rates (a_g) to choose a suitable marker to capture the heat release rate. A diffusion flame is established between two nozzles that are 10 cm apart from each other. From one nozzle, unburnt gas from the catalytic stage is supplied, and the air is supplied from the other nozzle. Fig. 10 shows that the peak locations of heat release rate (HRR) and OH profiles are slightly apart at a low strain rate ($a_g = 50$ sec^{-1}). The OH profile closely correlates with the HRR profile even at a high strain rate ($a_g = 300$ sec^{-1}). The separation between the peaks reduces when the O_2 percentage of the oxidizer stream reduces, and the OH profile matches the HRR profile closely. Thus, it can be concluded from counterflow 1-D simulations that the OH contours represent the heat release location with reasonable accuracy.

3.5.2. Instantaneous OH distribution

This section discusses the flame structure using planar laser-induced fluorescence (PLIF) of OH radicals. As stated in the previous section, the location of the heat release can be obtained from OH radical distribution. Fig. 11 shows the normalized instantaneous OH radical distribution at $O_2 = 21$ % and 13.13 %. It should be noted that PLIF images are taken at several axial locations for each experimental condition. In order to obtain a complete flame structure, we randomly choose instantaneous contours at different locations. For co-swirl, at $O_2 = 21$ %, radicals are distributed in the 'V'-shaped region, and large gradients in OH radicals can be found near the edge. In comparison, radicals are predominantly observed in the central region of the combustor for counter-swirl configuration. At $O_2 = 13.13$ %, radicals are distributed well over the combustor for both configurations. Thus, it can be concluded that the heat is released over a significantly large volume at a lower oxygen concentration. Fig. 11 also shows that the radicals are present in highly corrugated regions due to the turbulent nature of the flow. These wrinkled regions also indicate an excellent transport of heat and mass between inner and outer streams.

A stark difference is observed between OH*-chemiluminescence and PLIF images near the dump plane. The chemiluminescence signal is low close to the dump plane; however, PLIF images indicate the presence of OH radicals in significant quantity. This disparity is possibly due to the shape of the flame. The flame shape resembles an inverted cone, and the apex is located at the dump plane. As chemiluminescence provides line-of-sight integrated intensity, the signal close to the dump plane is low because of the smaller radius of the flame. The size of the flame increases downstream, which leads to an increase in the chemiluminescence

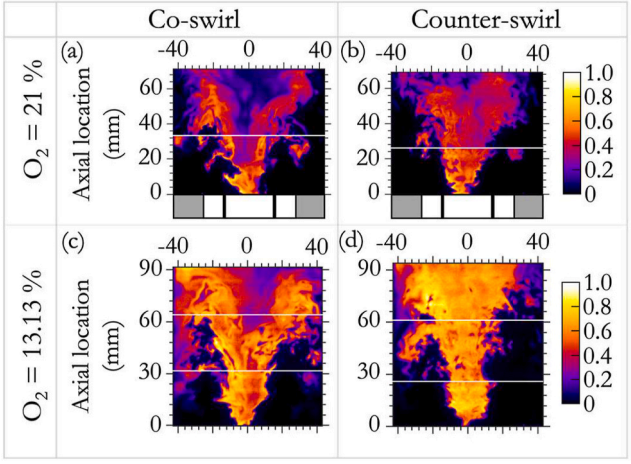

Fig. 11. The instantaneous OH distribution of co/counter swirl configurations at O_2 = 21 % and 13.13 % (each contour is normalized by its maximum intensity).

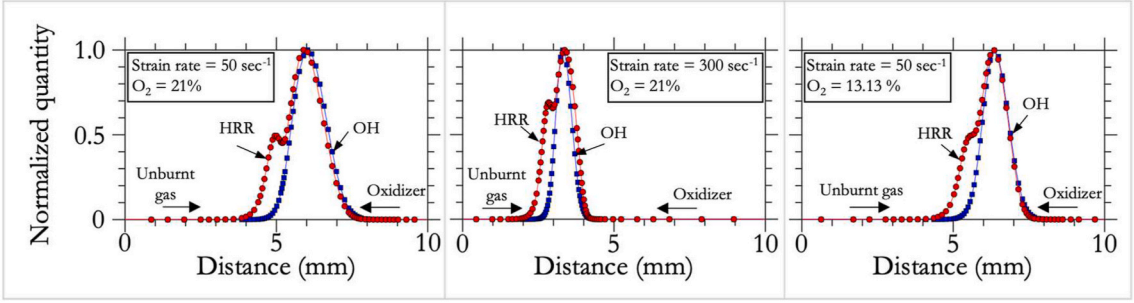

Fig. 10. The OH and heat release rate (HRR) profiles at a global strain rate of 50 sec^{-1} and 300 sec^{-1} and O_2 concentrations of 21 % and 13.13 %.

signal.

3.5.3. Mean OH distribution and velocity field

Fig. 12 shows the mean OH-radical distribution and velocity field of co/counter-swirl flames. The intensity is normalized by the peak intensity found at $O_2 = 21$ % in order to investigate the change in intensity with O_2 concentration. Fig. 12 indicates a reduction in OH intensity which corroborates the finding using chemiluminescence. PLIF images also confirm that the OH distribution is volumetric for both configurations, making the co/counter-swirl flames suitable for achieving MILD combustion.

The flow field of co/counter-swirl flames is discussed thoroughly in this section, as both flames show completely different flame topologies. At $O_2 = 21$ %, the co-swirl creates a flow field comprising a long slender central recirculation zone (CRZ) and an outer recirculation zone (ORZ). Near the dump plane, the radicals are present primarily inside the CRZ, which spans ~20 mm in the radial direction. No OH radicals can be found in ORZ because it is mainly filled with air or a mixture of air and product gases. No drastic change in the flow field is observed when oxygen concentration is reduced to 13.13 %. However, in order to assess the change in the strength of CRZ, we obtained recirculation ratio (*re*) at two O_2 concentrations. The value of *re* is defined as the ratio of recirculated (Q_{re}) and incoming (Q_{in}) volume flowrate, where the recirculated volume flow rate is obtained from axial velocity profiles using the following relation [59],

$$Q_{re} = \int_{-r^*}^{+r^*} -\pi \times r \times \overline{U}_x \, dr \tag{2}$$

$$re = Q_{re}/Q_{in} \tag{3}$$

where, $\overline{U}_x$ is the average axial velocity and it is negative between radial location $+r^*$ and $-r^*$. Here, we assume that the velocity profile is axisymmetric. Fig. 13(a) shows the variation in the recirculation ratio for co-swirl flames. The peak occurs at axial location (x) ~ 24 mm for $O_2 = 21$ %. The strength of the recirculation reduces, and the peak location shifts downstream when oxygen concentration reduces to 13.13 %.

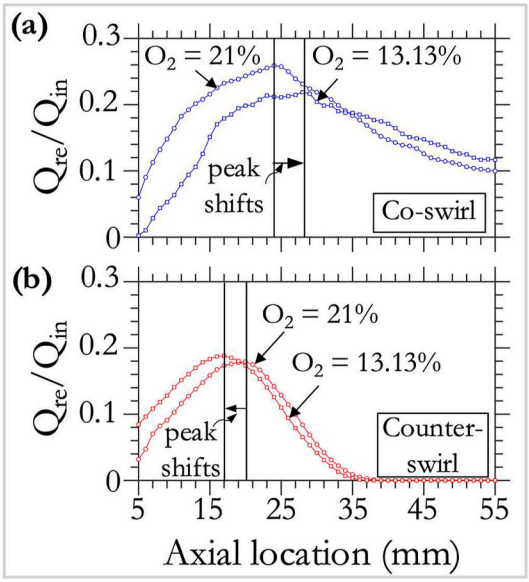

Fig. 13. (a) and (b) the variation of recirculation ratio (*re*) for co-swirl and counter-swirl flames, respectively.

In comparison, the counter-swirl configuration generates an entirely different flow field (as shown in Fig. 12(b) and **(d)**). At $O_2 = 21$ %, the flow field consists of a small ellipsoidal recirculation zone (RZ) which has a maximum radius of ~15 mm and spans ~40 mm in the axial direction. Near the dump plane, inner and outer streams mix vigorously because of the opposite swirling direction. This significantly reduces tangential momentum and generates a strong adverse pressure gradient along the combustor centerline. Flow recirculates under the influence of the adverse pressure gradient. As a result, a small recirculation zone is found near the dump plane. Fig. 12(b) also shows that the RZ zone is

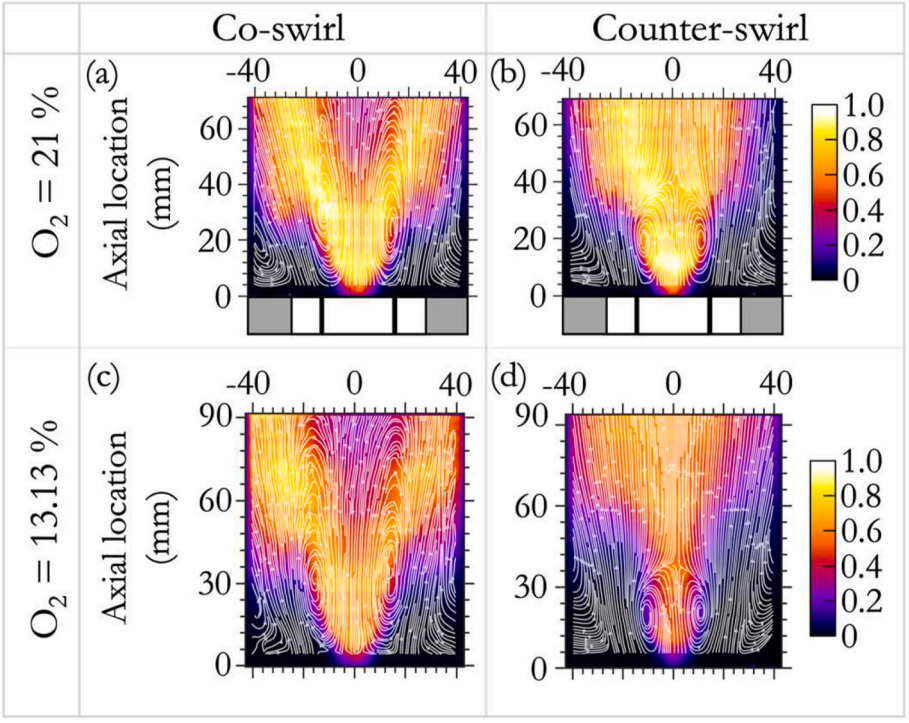

Fig. 12. The average OH contours and streamlines for co/counter-swirl flames at $O_2 = 21$ % and 13.13 % (Intensity is normalized with the maximum intensity found at $O_2 = 21$ %).

filled with OH radicals. Far from the downstream ($x > 40$ mm), no recirculation zone can be found. Although the overall flow field did not alter significantly, the size of the RZ slightly reduced at $O_2 = 13.13$ %. From Fig. 13(b), it is inferred that the trend of *re* is entirely different from co-swirl flames. The peak location shifts away from the dump plane for co-swirl when O_2 reduces. In contrast, the peak moves towards the dump plane for counter-swirl, and the peak value of *re* is higher than that observed at $O_2 = 21$ %.

As stated in the previous section, the differences in flame shape, height, and stand-off distance strongly depend on the velocity field generated by the co/counter-swirl configuration. The shape of the recirculation zone plays an important role in determining the flame shape. Near the dump plane, the reaction rate and recirculation ratio impact the flame stabilization. The reaction rate reduces in an oxygen-deficit environment, which makes the flame base susceptible to quenching. Thus, the flame stabilizes away from the dump plane. On the other hand, the recirculation of product gases promotes combustion and tries to stabilize the flame near the dump plane. These two opposing effects determine the flame stand-off height. In the case of co-swirl configuration, the strength of RZ reduces at low oxygen concentration, which leads to a higher stand-off height. However, for counter-swirl, the strength of RZ increases which tries to stabilize the flame base near the dump plane and counteract the effect of the reaction rate. As a result, the stand-off height slowly increases for counter-swirl compared to co-swirl.

Apart from the velocity field and OH-PLIF intensity, fine structures are investigated by calculating the gradient of OH-PLIF intensity. The gradient of the OH-PLIF is investigated from each instantaneous image in order to observe the fine structure in the flame. The gradient is calculated using the following relation,

$$\nabla I = \sqrt{\left(\frac{\partial I}{\partial x}\right)^2 + \left(\frac{\partial I}{\partial y}\right)^2} \tag{4}$$

Where I is the OH-PLIF intensity of the OH-PLIF signal. Fig. 14 (a) and **(b)** show the instantaneous PLIF image and its corresponding gradient in the entire domain. For all cases, even in MILD conditions, fine structures are observed near the dump plane. However, the maximum gradient decreases for both configurations when the oxygen concentration decreases. The probability distribution of the maximum gradient in the entire field (∇I_{max}) is obtained from 200 instantaneous images. The primary observation is that the maximum gradient decreases and the distribution narrows when O_2 changes to 13.13 % for both co and counter-swirl configurations. Thus, OH-PLIF indicates that the localization of the heat release region progressively decreases when oxygen concentration decreases.

In summary, the OH radical distribution and flow field of co/counter-swirl configuration are investigated using PLIF and PIV. The velocity field explains several vital differences between co and counter-swirl configurations. The PLIF images confirm that the radicals are distributed over a significant portion of the combustor for both configurations at low O_2 concentrations. The radical distribution proves the feasibility of achieving MILD combustion using a co/counter-swirl configuration.

3.6. Emissions at the exit of the combustor

The volumetric nature of the heat release rate is of little importance if the emission at the combustor exit is high. Thus, we investigate the impact of O_2 concentration on CO and NO_x emissions. The NO_x emission normalized by the 15 % O_2 is below 2 ppm for all conditions. At conventional conditions ($O_2 = 21$ %), a low NO_x emission is expected as the equivalence ratio in the swirl stage is low (~0.49). The flame temperature is also low because of such a low equivalence ratio. Dolai et al. [42] found that the peak temperature is lower than 1400 K, which is significantly lower than the critical temperature for the production of thermal NO_x. The flame temperature reduces gradually with the reduction in O_2. Thus, the lower oxygen concentration is more favorable for achieving ultra-low NO_x emission. However, the reduction in flame temperature affects the consumption rate of CO. The normalized CO emission is low (~10 ppm) at $O_2 = 21$ %. However, the emission slowly increases till $O_2 = 15.75$ % for both configurations (see Fig. 15). Then, a three-fold rise in CO emission is observed when the O_2 concentration is reduced to 13.13 %. While comparing co-swirl with counter-swirl flame, the co-swirl flame produces lower CO emissions at all oxygen percentages. Thus, the co-swirl configuration is preferable compared to the counter-swirl for achieving MILD combustion.

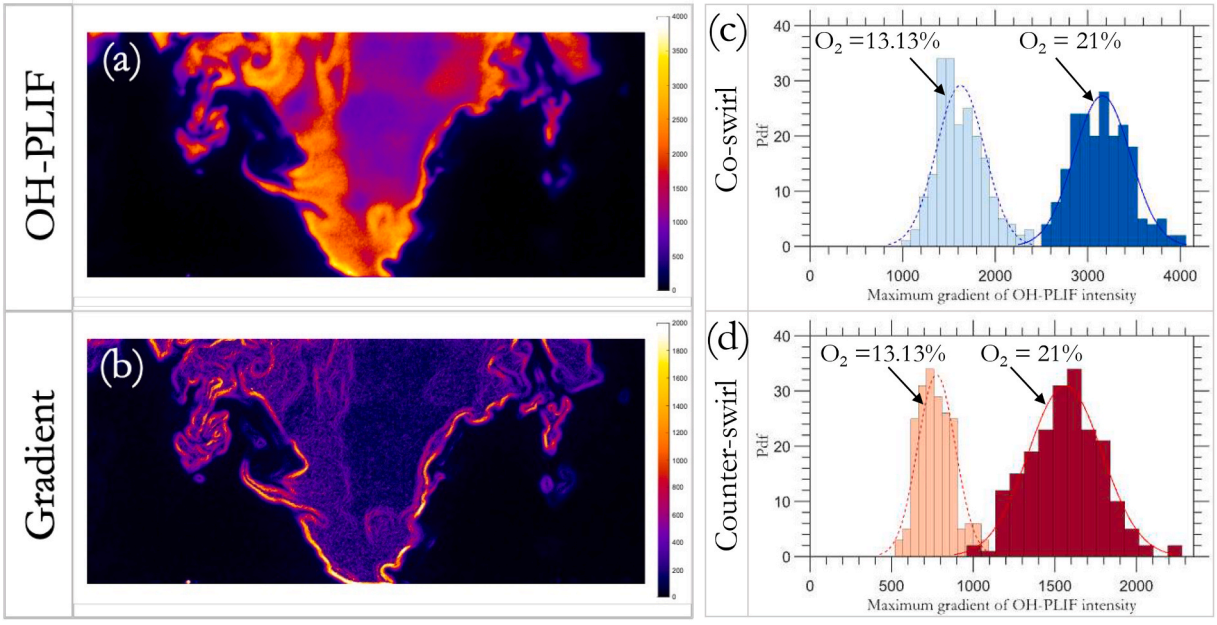

Fig. 14. (a) The instantaneous OH-planar laser-induced fluorescence image for co-swirling flames when $O_2 = 21$ %, (b) the gradient of OH-PLIF intensity of the same instantaneous image, **(c)** and **(d)** the distribution of maximum gradient obtained from 200 instantaneous images.

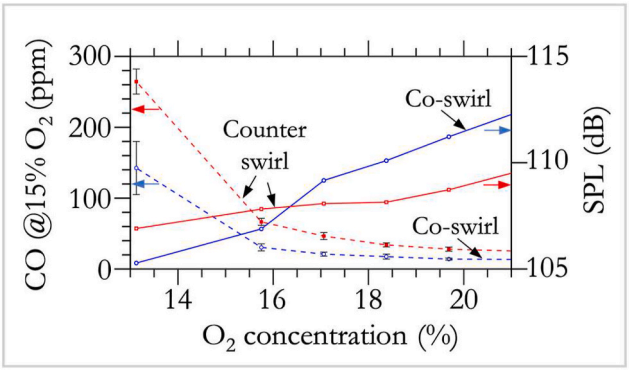

Fig. 15. The effect of O_2 concentration on CO emissions and sound pressure level (dB) for co/counter-swirl configuration (solid line → SPL and dashed line → CO).

3.7. Sound emitted by the combustor

Fig. 15 shows the trend of sound pressure level (SPL) measured using the microphone. The SPL is obtained from time series data (duration = 10 s) acquired at a frequency of 50 kHz. The decibel level is obtained using the following equations,

$$p = v_{rms}/s \tag{5}$$

$$dB = 20\log_{10}\frac{p}{p_o} \tag{6}$$

where v_{rms} is the root mean square (RMS) of the voltage recorded by NI-DAQ, s is the sensitivity of the instrument (Volts/Pa), and p_o is the reference pressure (20 μPa). For co-swirl configurations, the SPL shows a decreasing trend. The SPL level is ~112 dB at $O_2 = 21$ %, then gradually decreases to 109 dB when O_2 changes to 17.10 %. Then a sharp drop in decibel level (~3 dB) is observed as O_2 reduces to 15.75 %. The SPL level reduces even further at $O_2 = 13.13$ %. It is found that the SPL reduces by nearly 7 dB when O_2 is reduced from 21 % to 13.13 %. In comparison, the SPL decreases slowly for the counter-swirl configuration. The SPL falls gradually from ~109 dB to ~106 dB. The reduction in SPL is only by 3 dB, half of the reduction observed in co-swirl configurations. The SPL trend can be explained by examining the unsteadiness of the combustion. The pressure fluctuation inside the combustor is generated due to the unsteady heat release. Thus, any reduction in SPL indicates the steadiness of the combustion process. We utilized the standard deviation (SD) of chemiluminescence images and the averaged global intensity ($I(t)$) to assess the steadiness of combustion. As stated in the previous section, the SD decreases when O_2 concentration reduces, and this reduction in SD confirms that the steadiness of the combustion increases. Similarly, the distribution of $I(t)$ also provides information about the steadiness of combustion. The spread of $I(t)$ decreases with O_2, indicating that the combustion process becomes steadier with O_2 reduction. Similar to SPL, the value of SD reduces more for co-swirl configuration.

3.8. Power spectral density of sound data and OH* chemiluminescence

This section discusses the frequency spectrum of sound data emitted from the combustor to augment the understanding of the combustion process under a low O_2 environment. Fig. 16 shows the frequency spectrum corresponding to sound and average global luminosity ($I(t)$) for the co-swirl configuration. At $O_2 = 21$ %, the sound contains a dominant frequency (f_s) at ~287 Hz. The same dominant frequency is also present at $O_2 = 18.38$ %; however, the amplitude of the peak reduces. At $O_2 = 15.75$ %, no single dominant frequency is observed; instead, few clusters can be found between 200 Hz and 600 Hz. The amplitude corresponding to these clusters reduces even further at $O_2 = 13.13$ %. Thus, the amplitude of f_s shows a similar trend as SPL confirming a direct correlation between amplitude and SPL. The corresponding frequency spectrum obtained from high-speed OH* chemiluminescence is also shown in Fig. 15. At $O_2 = 21$ %, a dominant frequency (f_{ch}) is found at ~275 Hz, close to the dominant frequency (f_s) found in sound measurement. The heat release rate fluctuates approximately in periodic motion as the OH* intensity strongly correlates with the heat release rate (HRR). The fluctuation in heat release provides energy, which is exciting few modes of the combustor. If we consider the combustor as a quarter-wave resonator and the temperature inside the combustor is 1000 K, then the fundamental frequency of the axial mode is ~230 Hz, which is close to the f_s and f_{ch}. Thus, it can be concluded that the unsteady combustion process excites the axial mode of the combustor. The unsteadiness of the combustion process decreases with O_2 concentration, and no dominant peak can be found at $O_2 = 15.75$ % and 13.13 %. As the combustion process drives the pressure fluctuation, the SPL reduces with O_2 reduction because of the reduction in OH concentration, homogenization of the heat release region, and reduction in heat release fluctuation [60]. However, it should be noted that the combustion process may excite several modes other than axial mode, which will be studied in the future.

Fig. 17 shows the frequency spectrum of sound and $I(t)$ for counter-swirl configuration. The frequency spectrum is more complex compared to the co-swirl counterpart. At $O_2 = 21$ %, a dominant frequency (f_s) is observed at ~284 Hz. The location of the dominating frequency is the

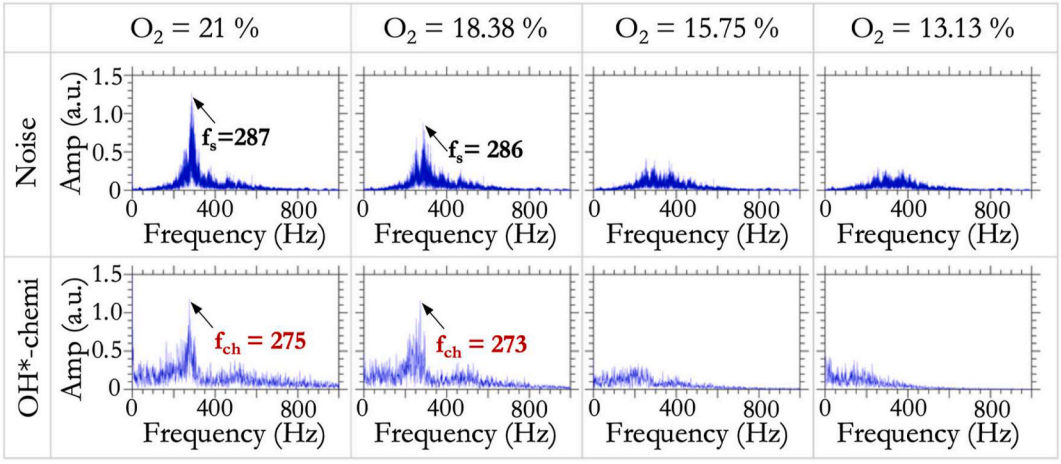

Fig. 16. The frequency spectrum of sound measurement and global luminosity ($I(t)$) for co-swirl at four O_2 percentages (f_s → dominant frequency of noise data, f_{ch} → dominating frequency of $I(t)$).

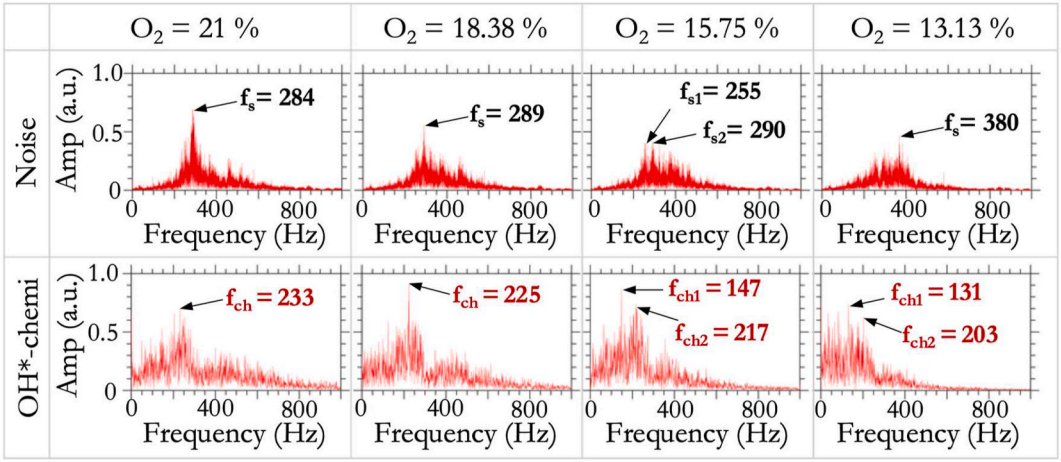

Fig. 17. The frequency spectrum of sound and global luminosity ($I(t)$) for counter-swirl (f_s → dominant frequency of noise data, f_{ch} → dominating frequency of $I(t)$).

same for co and counter-swirl flames. The corresponding frequency domain of $I(t)$ does not contain a definite dominant frequency. A cluster of peaks is located around 233 Hz, close to the dominant frequency (f_s) found in sound measurement. When the O_2 percentage is 18.38 %, the noise data has a dominant peak around 289 Hz, and the amplitude is slightly lower than that observed at O_2 = 21 %. The corresponding chemiluminescence has a dominant peak at ~233 Hz. However, the frequency domain contains a large cluster of small peaks. As the O_2 percentage decreases to 15.75 %, several clusters of peaks emerge at ~255, 290, 400, and 420 Hz. The amplitude of these peaks is comparable to the dominating frequency found at 18.38 %. The change in peak amplitude is not as prominent as in the co-swirl configuration. The corresponding frequency domain for chemiluminescence is similar to higher O_2 concentrations, and a peak is observed near 147 Hz. As the O_2 percentage reduces further to 13.13 %, the amplitude of the peaks near 255 Hz and 290 Hz decreases. The corresponding frequency spectrum of $I(t)$ shows several peaks within ~300 Hz. A direct correlation between chemiluminescence and sound measurement is not observed for the counter-swirl configuration, which needs further investigation. It should also be noted that the frequency domain analysis does not retain any information with time. Thus, a thorough analysis of noise data and chemiluminescence data is required to understand the dynamics in greater detail. Furthermore, the noise originating from the combustion can be comprised of both direct and indirect noise. At higher oxygen concentrations, the fluctuation in heat release rate generates temperature fluctuation, which can produce entropy waves [61]. As the global fluctuation is suppressed in MILD conditions, a detailed study of entropy waves can provide a useful understanding of indirect noise when combustion mode in MILD. Thus, a detailed investigation of combustion dynamics, along with entropy generation, will be presented in our future study.

3.9. Assessment of co/counter-swirl configuration for achieving MILD combustion

We considered five criteria to distinguish MILD mode from conventional combustion mode. During MILD combustion, the heat release zone should be volumetric, and the flame luminosity should be low [8, 28]. Besides luminosity, the combustion stability should be higher than conventional combustion [8,62]. The sound pressure level (SPL) and emissions should also be low [40]. By reviewing all these criteria, it can be concluded that the MILD combustion regime is achieved in co/counter-swirl configurations by reducing the oxygen concentration of the oxidizer stream. Both configurations show a reduction in OH* chemiluminescence intensity with O_2 concentration. The global luminosity suggests that the reduction of intensity is higher for the co-swirl compared to the counter-swirl configuration. However, it should be mentioned that the flames were neither colorless, invisible, nor transparent. The combustion mode is considered as MILD mode because of the low oxygen level. The PLIF images confirm the distributed nature of the combustion at low oxygen concentrations for both configurations. The combustion stability has improved for both configurations at lower O_2 concentrations. However, the co-swirl configuration shows higher stability than the counter-swirl. The sound pressure level (SPL) reduces for both configurations, and the lowest decibel level is observed for the co-swirl configuration at O_2 = 13.13 %. The NO_x emission is found to be below 2 ppm for all studied conditions. One drawback of the O_2 reduction is the trend of increasing CO emissions. However, compared to the counter-swirl configuration, the co-swirl configuration exhibits lower emissions for all studied conditions. Thus, we qualitatively conclude that MILD combustion can be achieved in the non-premixed mode at lower O_2 concentration and that the co-swirl configuration is preferable to the counter-swirl configuration.

4. Conclusions

The present study assesses the feasibility of achieving the MILD combustion regime in a co/counter-swirl configuration by reducing the oxygen concentration of the oxidizer stream from 21 % to 13.13 %. We investigated the flame structure, stability, emission, and sound pressure level (SPL) using high-speed OH*-chemiluminescence (5 kHz), planar laser-induced fluorescence (PLIF), two-dimensional particle image velocimetry (2D-PIV), species measurement, and sound measurement using a microphone. In the context of MILD combustion, the key findings of the work are the following.

1) The OH* chemiluminescence intensity decreases with the O_2 concentration. The mean intensity decreases by ~53 % for co-swirl when O_2 changes from 21 % to 13.13 %. In comparison, the intensity decreases only by ~23 % for the counter-swirl configuration. It should be mentioned that the flame was neither flameless nor colorless, even though the intensity was reduced significantly.
2) The unsteadiness of the combustion process is assessed using the standard deviation (SD) of chemiluminescence intensity and global intensity ($I(t)$). SD decreases for both configurations; however, the reduction for the co-swirl configuration is profound. A similar conclusion can be drawn from the $I(t)$ distribution. A small standard deviation of $I(t)$ indicates the stability of the combustion process. The standard deviation of global intensity ($I(t)$) reduces for co-swirl flames, whereas it remains approximately unchanged for counter-swirl flames, which implies that the co-swirl flame becomes more stable at lower O_2 concentrations.

3) The mean OH-PLIF images indicate the distributed nature of the combustion. Radicals occupy a substantially larger volume of the combustor at a low O_2 percentage.
4) The sound pressure level (SPL) decreases for both configurations with a reduction in O_2 percentage. The reduction in SPL for the co-swirl flame is almost twice of that observed with the counter-swirl flame.
5) The NO_x emission (@15 % O_2) is below 2 ppm for all conditions. The CO emission shows an increasing trend when the O_2 percentage is reduced for both configurations.
6) The frequency domains of sound and global luminosity (*I(t)* confirm that the combustion is exciting the fundamental axial mode of the combustor at O_2 = 21 %. At high oxygen concentrations, the frequency spectrums show a dominant frequency near ~280 Hz. However, the corresponding amplitude decreases with O_2 concentration. At O_2 = 13.13 %, no dominant frequency can be found for both sound and chemiluminescence measurements, which indicates that low-oxygen dilution combustion can be an effective strategy to decouple the unsteady heat-release rate and combustor acoustics.

Furthermore, the present study highlights a few differences between co and counter-swirling flames. The key differences are the following.

1) The co and counter-swirl flames exhibit completely different velocity fields. The co-swirl creates a long spindle-shaped recirculation zone (RZ), whereas the counter-swirl configuration generates a small ellipsoidal RZ near the dump plane. The recirculation ratio decreases for co-swirl and increases for counter-swirl configuration when oxygen concentration decreases.
2) Although the flame height and stand-off height increase for both configurations, the trend differs for co and counter-swirl configurations.
3) The co-swirl flames produce lower CO emissions at all conditions than the counter-swirl flames.

Thus, the present study, for the first time, successfully demonstrated MILD combustion in co/counter-swirl configurations using syngas as a fuel, and the co-swirl configuration is preferable compared to the counter-swirl configuration. Additionally, several differences between co and counter-swirling flow fields are presented.

Declaration of competing interest

The authors declare that they have no known competing financial interests or personal relationships that could have appeared to influence the work reported in the paper.

Acknowledgments

The authors like to acknowledge Dr. Prasad Boggavarapu for helping during the experiments. The authors also thank Dr. Santanu Pramanik and Dr. Pabitra Badhuk for several helpful discussions.

References

[1] Steele RC, Malte PC, Nicol DG, Kramlich JC. NOx and N2O in lean-premixed jet-stirred flames. Combust Flame 1995;100:440–9. https://doi.org/10.1016/0010-2180(94)00070-9.
[2] Roy Chowdhury B, Cetegen BM. Experimental study of the effects of free stream turbulence on characteristics and flame structure of bluff-body stabilized conical lean premixed flames. Combust Flame 2017;178:311–28. https://doi.org/10.1016/j.combustflame.2016.12.019.
[3] Zhao D, Gutmark E, de Goey P. A review of cavity-based trapped vortex, ultra-compact, high-g, inter-turbine combustors. Prog Energy Combust Sci 2018;66:42–82. https://doi.org/10.1016/j.pecs.2017.12.001.
[4] Krishna S, Ravikrishna RV. Optical diagnostics of fuel-air mixing and vortex formation in a cavity combustor. Exp Therm Fluid Sci 2015;61:163–76. https://doi.org/10.1016/j.expthermflusci.2014.10.012.
[5] Krishna S, Ravikrishna RV. Quantitative OH planar laser induced fluorescence diagnostics of syngas and methane combustion in a cavity combustor. Combust Sci Technol 2015;187:1661–82. https://doi.org/10.1080/00102202.2015.1047015.
[6] Gupta M, Pramanik S, Ravikrishna RV. Development of a syngas-fired catalytic combustion system for hybrid solar-thermal applications. Appl Therm Eng 2016;109:1023–30. https://doi.org/10.1016/j.applthermaleng.2016.04.150.
[7] Pramanik S, Ravikrishna RV. Numerical study of rich catalytic combustion of syngas. Int J Hydrogen Energy 2017;42:16514–28. https://doi.org/10.1016/j.ijhydene.2017.05.155.
[8] Pramanik S, Ravikrishna RV. Effect of N2 dilution and preheat temperature on combustion dynamics of syngas in a reverse-flow combustor. Exp Therm Fluid Sci 2020;110. https://doi.org/10.1016/j.expthermflusci.2019.109926.
[9] Bobba MK. Flame stabilization and mixing characteristics in a stagnation point reverse flow combustor. PhD Thesis. Atlanta: Georgia Institute of Technology; 2007.
[10] Bobba MK, Gopalakrishnan P, Periagaram K, Seitzman JM. Flame structure and stabilization mechanisms in a stagnation point reverse flow combustor. Proceedings of the ASME Turbo Expo 2007;2:879–88. https://doi.org/10.1115/GT2007-28231.
[11] Perpignan AAV, Gangoli Rao A, Roekaerts DJEM. Flameless combustion and its potential towards gas turbines. Prog Energy Combust Sci 2018;69:28–62. https://doi.org/10.1016/j.pecs.2018.06.002.
[12] Wuenning JA, Wuenning JG. Flameless oxidation to reduce thermal {NO}-formation. Prog Energy Combust Sci 1997;23:81–94.
[13] Arghode VK, Gupta AK, Bryden KM. High intensity colorless distributed combustion for ultra low emissions and enhanced performance. Appl Energy 2012;92:822–30. https://doi.org/10.1016/j.apenergy.2011.08.039.
[14] Arghode VK, Gupta AK. Effect of flow field for colorless distributed combustion (CDC) for gas turbine combustion. Appl Energy 2010;87:1631–40. https://doi.org/10.1016/j.apenergy.2009.09.032.
[15] Tsuji Hiroshi, Gupta Ashwani K, Hasegawa Toshiaki, Masashi Katsuki, Kishimoto Ken MM. High temperature air combustion: from energy conversion to pollution reduction. Boca Raton: CRC Press; 2002.
[16] Dally BB, Karpetis AN, Barlow RS. Structure of turbulent non-premixed jet flames in a diluted hot coflow. Proc Combust Inst 2002;29:1147–54. https://doi.org/10.1016/S1540-7489(02)80145-6.
[17] Oldenhof E, Tummers MJ, van Veen EH, Roekaerts DJEM. Role of entrainment in the stabilisation of jet-in-hot-coflow flames. Combust Flame 2011;158:1553–63. https://doi.org/10.1016/j.combustflame.2010.12.018.
[18] Arndt CM, Gounder JD, Meier W, Aigner M. Auto-ignition and flame stabilization of pulsed methane jets in a hot vitiated coflow studied with high-speed laser and imaging techniques. Appl Phys B 2012;108:407–17. https://doi.org/10.1007/s00340-012-4945-5.
[19] Gopalakrishnan P, Bobba MK, Seitzman JM. Controlling mechanisms for low NOx emissions in a non-premixed stagnation point reverse flow combustor. Proc Combust Inst 2007;31 II:3401–8. https://doi.org/10.1016/j.proci.2006.07.256.
[20] Pramanik S, Ravikrishna RV. Detached Eddy Simulation of syngas combustion in a reverse-flow configuration. Int J Hydrogen Energy 2020;45:27846–63. https://doi.org/10.1016/j.ijhydene.2020.07.058.
[21] Khalil AEE, Gupta AK. On the flame-flow interaction under distributed combustion conditions. Fuel 2016;182:17–26. https://doi.org/10.1016/j.fuel.2016.05.071.
[22] Khalil AEE, Gupta AK. Swirling flowfield for colorless distributed combustion. Appl Energy 2014;113:208–18. https://doi.org/10.1016/j.apenergy.2013.07.029.
[23] Medwell PR, Kalt PAM, Dally BB. Simultaneous imaging of OH, formaldehyde, and temperature of turbulent nonpremixed jet flames in a heated and diluted coflow. Combust Flame 2007;148:48–61. https://doi.org/10.1016/j.combustflame.2006.10.002.
[24] Medwell PR, Kalt PAM, Dally BB. Reaction zone weakening effects under hot and diluted oxidant stream conditions. Combust Sci Technol 2009;181:937–53. https://doi.org/10.1080/00102200902904138.
[25] Proud DB, Evans MJ, Kildare JA, Chan QN, Medwell PR. Pressurised combustion in hot and low-oxygen environments: chemiluminescence imaging and modelling. Fuel 2023;349. https://doi.org/10.1016/j.fuel.2023.128538.
[26] Mousavi SM, Sotoudeh F, Jun D, Lee BJ, Esfahani JA, Karimi N. On the effects of NH3 addition to a reacting mixture of H2/CH4 under MILD combustion regime: numerical modeling with a modified EDC combustion model. Fuel 2022;326. https://doi.org/10.1016/j.fuel.2022.125096.
[27] Li P, Wang F, Mi J, Dally BB, Mei Z. MILD combustion under different premixing patterns and characteristics of the reaction regime. Energy Fuel 2014;28:2211–26. https://doi.org/10.1021/ef402357t.
[28] Veríssimo AS, Rocha AMA, Costa M. Operational, combustion, and emission characteristics of a small-scale combustor. Energy Fuel 2011;25:2469–80. https://doi.org/10.1021/ef200258t.
[29] Mahendra Reddy V, Sawant D, Trivedi D, Kumar S. Studies on a liquid fuel based two stage flameless combustor. Proc Combust Inst 2013;34:3319–26. https://doi.org/10.1016/j.proci.2012.06.028.
[30] Sharma S, Chowdhury A, Kumar S. Effect of CO2/N2 dilution on characteristics of liquid fuel combustion in flameless combustion mode. Combust Sci Technol 2020. https://doi.org/10.1080/00102202.2020.1780582.
[31] Pramanik S, Ravikrishna RV. Non premixed operation strategies for a low emission syngas fuelled reverse flow combustor. Energy 2022;254:124332. https://doi.org/10.1016/j.energy.2022.124332.
[32] Li P, Wang F, Mi J, Dally BB, Mei Z, Zhang J, et al. Mechanisms of NO formation in MILD combustion of CH4/H2 fuel blends. Int J Hydrogen Energy 2014;39:19187–203. https://doi.org/10.1016/j.ijhydene.2014.09.050.

[33] Cavaliere A, de Joannon M. Mild combustion. Prog Energy Combust Sci 2004;30:329–66. https://doi.org/10.1016/j.pecs.2004.02.003.
[34] Dolai A, Pramanik S, Badhuk P, Ravikrishna RV. Nonlinear dynamic analysis of the transition from MILD regime to thermoacoustic instability in a reverse flow combustor. Combust Sci Technol 2022;00:1–24. https://doi.org/10.1080/00102202.2022.2104608.
[35] Cheong KP, Wang G, Mi J, Wang B, Zhu R, Ren W. Premixed MILD combustion of propane in a cylindrical furnace with a single jet burner: combustion and emission characteristics. Energy Fuel 2018;32:8817–29. https://doi.org/10.1021/acs.energyfuels.8b01587.
[36] Coghe A, Solero G, Scribano G. Recirculation phenomena in a natural gas swirl combustor. Exp Therm Fluid Sci 2004;28:709–14. https://doi.org/10.1016/j.expthermflusci.2003.12.007.
[37] Khalil AEE, Gupta AK. Impact of internal entrainment on high intensity distributed combustion. Appl Energy 2015;156:241–50. https://doi.org/10.1016/j.apenergy.2015.07.044.
[38] Khalil AEE, Gupta AK. Towards colorless distributed combustion regime. Fuel 2017;195:113–22. https://doi.org/10.1016/j.fuel.2016.12.093.
[39] Feser JS, Karyeyen S, Gupta AK. Flowfield impact on distributed combustion in a swirl assisted burner. Fuel 2020;263:116643. https://doi.org/10.1016/j.fuel.2019.116643.
[40] Khalil AEE, Gupta AK. Acoustic and heat release signatures for swirl assisted distributed combustion. Appl Energy 2017;193:125–38. https://doi.org/10.1016/j.apenergy.2017.02.030.
[41] Zhang K, Shen Y, Duwig C. Identification of coherent structures in distributed swirl-stabilized wet combustion. Fuel 2021;296:120685. https://doi.org/10.1016/j.fuel.2021.120685.
[42] Dolai A, Badhuk P, Ravikrishna RV. Investigation of syngas combustion in a novel ultra-low emission 20-kW two-stage combustor. Fuel 2023:340. https://doi.org/10.1016/j.fuel.2023.127497.
[43] Dolai A, Ravikrishna RV. An experimental investigation of syngas combustion using a 26 kW two-stage combustor, 13th Asia Pacific Conference on Combustion. 2021.
[44] Huang Y, Yang V. Dynamics and stability of lean-premixed swirl-stabilized combustion. Prog Energy Combust Sci 2009;35:293–364. https://doi.org/10.1016/j.pecs.2009.01.002.
[45] Chen J, Liu B, Gao X, Yan L, Xu D. Effects of heterogeneous-homogeneous interaction on the homogeneous ignition in hydrogen-fueled catalytic microreactors. Int J Hydrogen Energy 2016;41:11441–54. https://doi.org/10.1016/j.ijhydene.2016.05.022.
[46] Smith G.P., Golden D.M., Frenklach M., Moriarty N. W., Eitenner B., Goldenberg B., Bowman C.T., Hanson R.K., Song S., Gadiner Jr W.C., Lissianski V.V., Qin Z., GRI-Mech 3.0. http://www.me.berkley.edu/gri_mech/.
[47] Lyubovsky M, Smith LL, Castaldi M, Karim H, Nentwick B, Etemad S, et al. Catalytic combustion over platinum group catalysts: fuel-lean versus fuel-rich operation. Catal Today 2003;83:71–84. https://doi.org/10.1016/S0920-5861(03)00217-7.
[48] Choudhary TV, Banerjee S, Choudhary VR. Catalysts for combustion of methane and lower alkanes, 234; 2002.
[49] Mantzaras J. Catalytic combustion of hydrogen, challenges, and opportunities. Advances in chemical engineering. 45. Academic Press Inc.; 2014. p. 97–157. https://doi.org/10.1016/B978-0-12-800422-7.00003-0.
[50] Persson K, Jansson K, Järås SG. Characterisation and microstructure of Pd and bimetallic Pd-Pt catalysts during methane oxidation. J Catal 2007;245:401–14. https://doi.org/10.1016/j.jcat.2006.10.029.
[51] Schultze M, Mantzaras J. Hetero-/homogeneous combustion of hydrogen/air mixtures over platinum: fuel-lean versus fuel-rich combustion modes. Int J Hydrogen Energy 2013;38:10654–70. https://doi.org/10.1016/j.ijhydene.2013.06.069.
[52] Reinke M, Mantzaras J, Schaeren R, Bombach R, Inauen A, Schenker S. High-pressure catalytic combustion of methane over platinum: in situ experiments and detailed numerical predictions. Combust Flame 2004;136:217–40. https://doi.org/10.1016/j.combustflame.2003.10.003.
[53] Bolaños-Chaverri F, Mantzaras J, Griffin T, Bombach R, Winkler D. An experimental and numerical investigation of the catalytic-rich/gaseous-lean combustion of H2/CO/air mixtures at 8 bar. Proc Combust Inst 2021;38:5443–51. https://doi.org/10.1016/j.proci.2020.06.149. Elsevier Ltd.
[54] Merkle K, Haessler H, Büchner H, Zarzalis N. Effect of co- and counter-swirl on the isothermal flow- and mixture-field of an airblast atomizer nozzle. Int J Heat Fluid Flow 2003;24:529–37. https://doi.org/10.1016/S0142-727X(03)00047-X.
[55] Turns SR, others. Introduction to combustion, 287. New York, NY, USA: McGraw-Hill Companies; 1996.
[56] Zhou B, Costa M, Li Z, Aldén M, Bai XS. Characterization of the reaction zone structures in a laboratory combustor using optical diagnostics: from flame to flameless combustion. Proc Combust Inst 2017;36:4305–12. https://doi.org/10.1016/j.proci.2016.06.182.
[57] Degenève A, Vicquelin R, Mirat C, Labegorre B, Jourdaine P, Caudal J, et al. Scaling relations for the length of coaxial oxy-flames with and without swirl. Proc Combust Inst 2019;37:4563–70. https://doi.org/10.1016/j.proci.2018.06.032.
[58] Sadanandan R, Chakraborty A, Arumugam VK, Chakravarthy SR. Optical and laser diagnostic investigation of flame stabilization in a novel, ultra-lean, non-premixed model GT burner. Combust Flame 2018;196:466–77. https://doi.org/10.1016/j.combustflame.2018.06.028.
[59] Degeneve A, Vicquelin R, Mirat C, Caudal J, Schuller T. Impact of co- and counter-swirl on flow recirculation and liftoff of non-premixed oxy-flames above coaxial injectors. Proc Combust Inst 2021;38:5501–8. https://doi.org/10.1016/j.proci.2020.06.279.
[60] Mousavi SM, Kamali R, Sotoudeh F, Pourabidi R, Karimi N, Jeung IS. A comprehensive investigation of acoustic power level in a moderate or intense low oxygen dilution in a jet-in-hot-coflow under various working conditions. Aero Sci Technol 2019;93. https://doi.org/10.1016/j.ast.2019.105339.
[61] Wang G, Liu X, Wang S, Li L, Qi F. Experimental investigation of entropy waves generated from acoustically excited premixed swirling flame. Combust Flame 2019;204:85–102. https://doi.org/10.1016/j.combustflame.2019.03.005.
[62] Pramanik S, Ravikrishna RV. Non premixed operation strategies for a low emission syngas fuelled reverse flow combustor. Energy 2022;254. https://doi.org/10.1016/j.energy.2022.124332.